AIAA Infotech@Aerospace Conference
and
AIAA Unmanned...Unlimited Conference
6 - 9 April 2009, Seattle, Washington

AIAA 2009-1929

Neurobiologically Inspired Control of Engineered Flapping Flight

Soon-Jo Chung*, Jeremiah R. Stoner†, and Michael Dorothy‡*
Iowa State University, Ames, Iowa, 50011, USA

This article presents a new control approach for engineered flapping flight with many interacting degrees of freedom. This paper explores the applications of neurobiologically inspired control systems in the form of Central Pattern Generators (CPG) to generate wing trajectories for potential flapping flight MAVs. We present a rigorous mathematical and control theoretic framework to design complex three dimensional motions of flapping wings. Most flapping flight demonstrators are mechanically limited in generating the wing trajectories. Because CPGs lend themselves to more biological examples of flight, a novel robotic model has been developed to emulate the flight of bats. This model has shoulder and leg joints totaling 10 degrees of freedom for control of wing properties. Results of wind tunnel experiments and numerical simulation of CPG-based flight control validate the effectiveness of the proposed neurobiologically inspired control approach.

Nomenclature

ϕ_w, ψ_w, θ_w	Flapping, lead-lag, and pitch angles of each wing (left, right)
$\mathbf{x}_i = (u_i, v_i)^T$	State vector of the i-th Hopf oscillator
$\mathbf{f}(\mathbf{x}_i; \rho_i)$	Hopf nonlinear equations in the vector form with radus ρ_i
ρ_i	Radius of the limit cycle from the i-th Hopf oscillator
λ	Common rate of convergence of Hopf oscillators
ω	Common oscillation frequency of Hopf oscillators, rad/s
a_i	Amplitude bias of the i-th Hopf oscillator
$\mathbf{R}(\Delta_{ij})$	2×2 rotational transformation matrix
Δ_{ij}	Phase lead of the i-th Hopf oscillator from the j-th
n	Total number of Hopf oscillators in the CPG network
$\mathbf{I}_k$	Identity matrix $\in \mathbb{R}^{k \times k}$
k	Coupling gain of the coupled Hopf oscillators
k_r	Reduced frequency of the flapping wing
ℓ	Contraction rate of the virtual nonlinear system
$\mathbf{G}$	Original Laplacian matrix with rotational transformation $\in \mathbb{R}^{2n \times 2n}$
$\mathbf{L}$	Graph Laplacian matrix $\in \mathbb{R}^{2n \times 2n}$
$\mathbf{V}$	Matrix of orthonormal eigenvectors of $\mathbf{L}$ without the ones vector $\in \mathbb{R}^{2n \times 2(n-1)}$
$\lambda_{min}(\cdot)$, $\lambda_{max}(\cdot)$	Minimum or maximum eigenvalues of the matrix
$\mathbf{x}_b = (x_b, y_b, z_b)$	Vehicle body frame coordinates
$\mathbf{x}_w = (x_w, y_w, z_s)$	Wing frame coordinates (left, right)
$\mathbf{x}_s = (x_s, y_s, z_s)$	Stroke plane frame coordinates
R	Wing span of a single wing, m
r	Wing span coordinate value $r \in [0, R]$ of the wing blade element
$\alpha_w(r, t)$	Local angle of attack of the wing blade element

*Assistant Professor of Aerospace Engineering, Senior Member AIAA, Phone: 515-294-5459, sjchung@alum.mit.edu.
†Graduate Research Assistant, Aerospace Engineering, jerry507@iastate.edu.
‡Research Assistant, Aerospace Engineering, mdorothy@iastate.edu.

$\beta_w(r,t)$	Local direction of the wind in the wing frame
V_∞	Speed of the vehicle, without the relative wind, m/s
V_r	Local wind speed of the wing blade element, m/s
$C_L(\alpha_w)$, $C_D(\alpha_w)$	Local lift and drag coefficients of the blade element
F_{wx}, F_{wz}	Total aerodynamic forces of each wing in the x and z directions of the wing frame
$\mathbf{F} = (F_x, F_y, F_z)^T$	Total aerodynamic forces from the wing in the body frame (left, right)
$\mathbf{d} = (d_x, d_y, d_z)^T$	Location of the stroke and wing frames with respect to the body frame
$\mathbf{T}_{bs}$, $\mathbf{T}_{sw}$	Angular transformation matrix
α_x, α_y	Angle of attack and slide-slip angle of the vehicle body, rad/s
$\mathbf{\Theta}_s$	Stroke plane inclination angle from the vertical line
$\mathbf{T}_{be}$	Directional cosine matrix of Euler angles $\in \mathbb{R}^{3\times3}$
$\mathbf{\Omega}_b = (p,q,r)^T$	Body angular rate, rad/s
$(\phi_b, \theta_b, \psi_b)$	Euler angles of the vehicle body with respect to the inertial frame, rad
$\mathbf{M} = (M_x, M_y, M_z)$	Total aerodynamic moments from each wing, Nm
$\mathbf{V}_b = (V_{bx}, V_{by}, V_{bz})^T$	Vehicle velocity vector in the body frame
$\mathbf{F}_g = (0,0,mg)^T$	Gravitational force vector in the inertial frame
$\mathbf{A} = (A_x, A_y, A_z)^T$	Additional forces generated by the body (fuselage) and the tail
$\mathbf{I}_b$	Inertia matrix $\in \mathbb{R}^{3\times3}$, kgm^2
$\mathbf{B} = (B_x, B_y, B_z)^T$	Additional aerodynamic moments from the body and the tail
Subscript	
i	Variable number of the coupled Hopf nonlinear oscillators
R, L	Right or left wing
b, s, w	Body, stroke, and wing frame

I. Introduction

Engineered flapping flight holds promise for creating biomimetic micro aerial vehicles (MAVs) flying in low Reynolds number regimes (Re$< 10^5$) where rigid fixed wings drop substantially in aerodynamic performance. MAVs are typically classified as having maximum dimensions of 15 cm and flying at a nominal speed of 1–20 m/s in tight urban environments.[1,2] Although natural flyers such as bats, birds, and insects have captured the imaginations of scientists and engineers for centuries, the maneuvering characteristics of man-made aircraft are nowhere near the agility and efficiency of animal flight.[3–5] Such highly maneuverable MAVs, equipped with intelligent sensors, will make paradigm-shifting advances in monitoring of critical infrastructures such as power grids, bridges, and borders, as well as in intelligence, surveillance, and reconnaissance applications. The successful reverse-engineering of flapping flight will potentially result in a transformative innovation in aircraft design, which has been dominated by fixed-wing airplanes.

The objective of this article is to investigate and evaluate the hypothesis that the adaptive control and synchronization of coupled nonlinear oscillators, inspired by central pattern generators (CPGs) found in animal spinal cords, can effectively produce and control biomimetic flapping flight (see Figure 1). An engineered CPG network, which ensures the stability and robust adaptation of motion, can significantly reduce the complexity associated with flapping flight. Unique to this research approach is the potential to reverse-engineer the key mechanisms of highly adaptive and robust rhythmic pattern modulations of flapping flight by integrating the neurobiological principles with the rigorous mathematical tools borrowed from nonlinear synchronization theory and flight dynamics and controls. Such an approach has not been adopted for engineered flapping flight.

Flapping flight in an efficient means of powered flight for MAVs flying in low Reynolds number regimes. Bats and birds effectively control their flight by flapping and flexing their wings, thereby delaying the stall of the wings at a high angle of attack without increasing their flight speed (see Figure 2). In particular, we focus onon the unparalleled robustness, adaptability, and agility of animal flight. For example, bats can fly with damaged wings (robustness) or while carrying 50 percent of their original weight (adaptation). Many insects can also carry loads exceeding their body weight.[6]

Central to the agile flight of natural flyers is the ability to execute complex synchronized three-dimensional motions of the wings as shown in Figure 2. In this paper, we introduce a mathematical framework based on CPG control theory that enables such synchronized wing maneuvers. While bats control the flexible

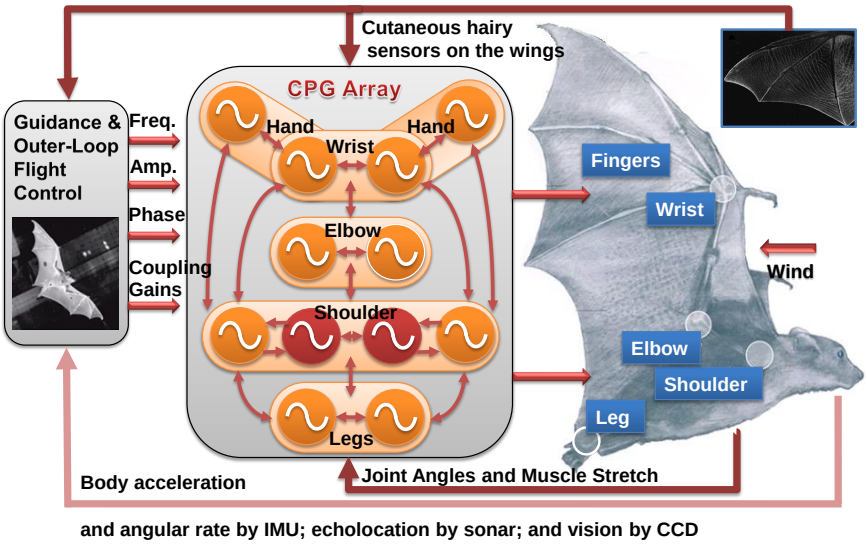

Figure 1. Proposed hierarchical control structures with the main controller and the CPG network. The outer-loop flight control modulates the rhythmic patterns (frequency, amplitude, phase lag, coupling gains) of the CPG network, without the need for directly controlling a multitude of joints.

membrane wings by more than 24 joints,[7,8] strict mimicry of such dimensionality is avoided. Hence, in this paper, we focus on three stereotyped motion primitives to define the three dimensional movements of wings: main flapping (stroke) motion (Fig. 2a), lead-lag motion (Fig. 2b), and wing pitch twisting (Fig. 2c). Studying such synchronized wing motions is expected to shed light on the key characteristics of animal flapping flyers.

I.A. Related Work

While unsteady aerodynamics of flapping flight in low Reynolds number regimes has been extensively studied through numerical[2,9–14] and experimental studies,[1,6,15–18] one of the most interesting and least understood aspects of bio-inspired flapping flight is how to precisely control and synchronize multiple limbs and joints that generate complex oscillatory movements of the wings in three dimensions. The research described in this article aims to overcome the technical barriers associated with the control of flapping flight which involves a large number of interacting degrees of freedom (see Figures 1 and 2). Previous robotic flapping flyers have one or two degrees of freedom in the wings.[6,14,16,19–28] However, even insects like the dragonfly (*Anax parthenope*) are reported to have complex three-dimensional movements by actively controlling flapping and twisting of four independent wings.[3]

In particular, as shall be seen later in this paper, the use of sinusoidal functions (e.g., $\theta(t) = \theta_0 + \sin(\omega t + \phi_0)$) to generate the oscillatory motions of the wings does not permit stable and agile flapping flying maneuvers especially with time-varying oscillation frequency and synchronization of multiple joints. Prior studies in flapping flight[1–3,5,7,8,11–13,15,18,27–30] assumed a very simple sinusoidal function for each joint to generate flapping oscillations, without deliberating on how multiple limbs (or their nervous systems) are connected and actuated to follow such a time-varying reference trajectory. In order to bridge this gap, this article aims to establish a novel adaptive CPG-based control theory for flapping flight, through neuromechanical modeling, nonlinear control and synchronization, and experimental evaluation.

To date, there have been few examples of flapping flight testbeds, with most systems designed at emulating insect flight and being large static testbeds. This paper presents a unique robotic test platform which permits the motion of the wing with five control variables per wing (8 degrees of freedom altogether). Previous examples of flapping wing mechanisms can be found in [16, 19, 22, 31–33] and in some commercial products such as the Dragonfly and the Cybird. All of these systems use a crankshaft mechanism to produce the flapping motions, and are therefore limited to producing the same sinusoidal motion of fixed amplitude for both wings. However, experimental results using high speed cameras have shown that the flapping motions in bats and birds are more complicated than perfect sinusoidal[3,17] with a fixed amplitude. However, prior

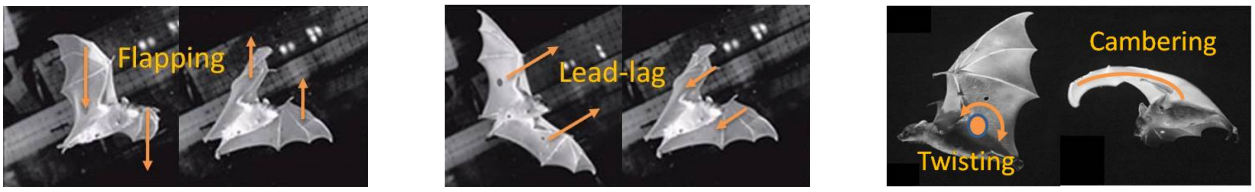

(a) flapping (ϕ_w) (b) lead-lag (ψ_w) (c) twisting (θ_w) and cambering)

Figure 2. Basic wing movements of bats (pictures from [18]). Except for cambering, birds exhibit similar wing movements. Twisting (pitching) changes the effective angle of attack while cambering changes the aerodynamic efficiency. The fingers and hind legs control the tension of the flexible membrane wings, which distinguish bats from birds.[5]

systems do not allow changes in flapping stroke amplitude as well as stroke frequency. Further, multiple parameters of the flapping change depending on flight conditions such as the pitch and the lead-lag angles (see Fig. 2). The amplitude of the wing beats varies, as does the phase relationship between the different movements of the wing.

The paper is organized as follows. We illustrate the fundamentals and advantages of the CPG based control for engineered flapping flight in Section II. We present a mathematical and control theoretic formulation of synchronized motions of multiple joints in the wings and body in Section II.B in the context of combining the CPG network with the kinematic modeling of three-dimensional multi-joint wings presented in Section III. We present results of simulations with with multijoint coordination that go beyond previous studies on robotic flapping flyers with a single-joint wing beating in Section IV. Further, we introduce a unique robotic flapping flying testbed in Section V and its experimental results that validate the proposed control strategy. We understand the challenges associated with building lightweight actuators to truly realize the potential of three dimensional wing maneuvers. We present the fundamental neurobiologically inspired control theory that can further contribute to engineered flapping flight, once such light-weight actuators become available in the future. In the meantime, we show how the multi-joint robotic bat testbed driven by CPG control can further enhance our understanding of biomimmetic flapping flight.

II. Fundamentals of Neurobiologically Inspired Control

This article reports the first investigation of CPG models by using coupled limit cycle oscillators for the purpose of controlled engineered flapping flight. The central pattern generators of animals are neural networks that can endogenously (i.e., without rhythmic sensory or central input) produce coordinated patterns of rhythmic outputs. Hence, CPGs are believed to reduce the computation burden of the brain. As seen in Fig. 1, the central controller, similar to the brain of an animal, can stabilize the vehicle dynamics by commanding a reduced number of variables such as the frequency and phase difference of the oscillators instead of directly controlling multiple joints. The existence of CPGs has been confirmed by biologists.[34–42] Interestingly, the first modern evidence of CPGs came from the experiments with *flapping flying locusts*[43] rather than walking or swimming animals. Experiments with limbed vertebrates have also shown that individual limbs can produce rhythmic movements endogenously.[38,44] Such empirical data have been interpreted as evidence that each limb has its own CPGs that can behave in a self-sustained way. However, sensory feedback is also known to play a crucial role in altering motor patterns[38,45] to cope with environmental perturbations. Incorporation of sensory feedback into the CPG model has been presented in [46] for a turtle robot.

The most popular animal model for CPGs has been the lamprey, a primitive eel-like fish.[47] While the robotics community eagerly embraced the concept of CPG models for swimming or walking robots,[46,48–50] this work reports the first CPG-based control for flapping flight. The use of nonlinear oscillators for insect flapping flight has also been suggested by some biologists.[29,30] Clearly, flapping flight is technically more challenging to mimic than swimming and walking, due to its uncompromising aerodynamic characteristics.

II.A. Robust and Adaptive Flapping Pattern Generation by CPGs

Our neurobiologically inspired approach centers on deriving an effective mathematical model of CPGs based on coupled nonlinear limit cycle dynamics. Once neurons form reciprocally inhibiting relations, they oscillate and spike periodically.[46] An abstract mathematical model of complicated neuron models can be obtained by

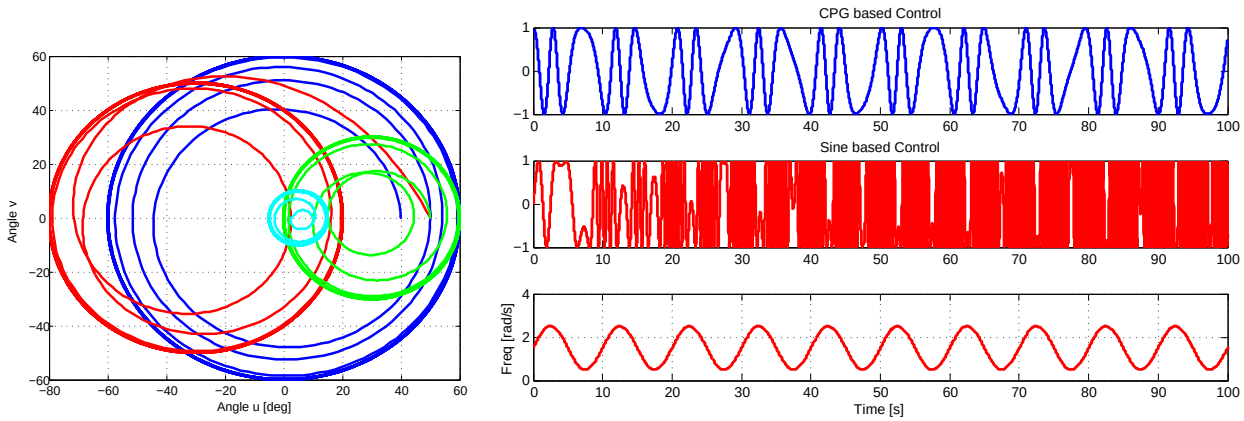

(a) (b)

Figure 3. (a) Phase portrait of multiple Hopf oscillators synchronizing (b)CPG-based control using Hopf limit cycle (first row) and $\sin(\omega t)$ control (second row) with time-varying $\omega(t)$ (third row). The Hopf limit cycle shows a much smoother transition. This is true for amplitude and bias changes as well.

coupled nonlinear limit cycles that essentially exhibit the rhythmic behaviors of coupled neuronal networks. In the field of nonlinear dynamics, a limit cycle is defined as an isolated closed trajectory that exhibits self-sustained oscillation.[51,52] If *stable*, small perturbations (initial conditions) will be forgotten and the trajectories will converge to the limit cycle (see Figures 3a and 3b). This superior robustness makes a limit cycle an ideal simplified dynamic model of CPGs.

In the present paper, we use the following limit-cycle model called the Hopf oscillator, named after the Hopf bifurcation model:

$$\frac{d}{dt}\begin{pmatrix} u-a \\ v \end{pmatrix} = \begin{bmatrix} -\lambda\left(\frac{(u-a)^2+v^2}{\rho^2}-1\right) & -\omega(t) \\ \omega(t) & -\lambda\left(\frac{(u-a)^2+v^2}{\rho^2}-1\right) \end{bmatrix}\begin{pmatrix} u-a \\ v \end{pmatrix} + \mathbf{u}(t) \tag{1}$$

$$\text{Equivalently,} \quad \dot{\mathbf{x}} = \mathbf{f}(\mathbf{x};\rho) + \mathbf{u}(t), \quad \text{with} \quad \mathbf{x} = (u-a, v)^T$$

where the $\lambda > 0$ denotes the convergence rate to the symmetric limit circle of the radius $\rho > 0$ and $\mathbf{u}(t)$ is an external or coupling input. Indeed, for a single Hopf oscillator with $\mathbf{u}(t) = 0$, a Lyapunov function $V = \left(\frac{(u-a)^2+v^2}{\rho^2} - 1\right)^2$ can be used to prove global asymptotic stability to the limit circle. For coupled Hopf oscillators, the stability proof is much more involved and discussed in Section II.B.

Also, the possibly time-varying parameter $\omega(t) > 0$ determines the oscillation frequency of the limit circle. Note that a constant or slowly varying a sets the bias to the limit cycle such that $u(t) = \rho\cos(\omega t + \delta) + a$ and $v(t) = \rho\sin(\omega t + \delta)$ on a circle. The variable output $u(t)$ is then used to to generate an oscillatory signal for the corresponding joint. Since it does not change the results of the stability proof, we will drop this bias "a" in the equations. Then, the output variable to generate the desired oscillatory motion of each joint is the first state u from the Hopf oscillator model in (1).

In order to construct an artificial CPG network, some prior work uses a discrete nonlinear equation that describes spiking and spiking-bursting of a neuron model.[48] On the other hand, the Hopf oscillator has been a popular dynamic model of the engineered CPG arrays (e.g., see the salamander robot[49,49] and the turtle robot[46]). The stability of coupled Hopf oscillators has been extensively investigated in [46,53,54]. One nice property of the Hopf oscillator in (1) is that its limit cycle is a symmetric circle as opposed to Van der Pol[34] or Rayleigh oscillators.[51] Further, as shall been seen later, the following two properties are exploited in the stability proof of phase synchronization:

$$\mathbf{f}(\mathbf{R}(\Delta)\mathbf{x};\rho) = \mathbf{R}(\Delta)\mathbf{f}(\mathbf{x};\rho) \quad \mathbf{R}(\Delta) = \begin{bmatrix} \cos\Delta & -\sin\Delta \\ \sin\Delta & \cos\Delta \end{bmatrix} \tag{2}$$

where $\mathbf{R}(\Delta) \in \mathcal{SO}(2)$ is a 2D rotational transformation such that $\mathbf{R}(-\Delta) = -\mathbf{R}(\Delta) = \mathbf{R}^{-1}(\Delta) = \mathbf{R}^T(\Delta)$. Also, its scaling factor can be expressed as

$$\mathbf{f}(g\mathbf{x};\rho) = g\mathbf{f}(\mathbf{x};\rho/g) \tag{3}$$

It is well known that birds and bats modulate their flapping frequency during their flight, while the flapping frequency of insects varies very little. If one uses a sinusoidal function $\phi_w = \sin(\omega t)$ to generate oscillatory patterns of the wing, the frequency variation for the purpose of flight control is not permitted as seen in Fig. 3b. This salient point is further illustrated in this section. The following advantages motivate the use of more sophisticated CPG-based control over conventional control approaches that use harmonic sinusoidal waves. The main advantages are (1) adaptive pattern modulation, (2) reduced dimensionality and bandwidth requirement, and (3) symmetric and symmetry-breaking oscillations

II.A.1. Key Advantage of CPG-based Control for Flapping Flight: Adaptive Pattern Modulation

Birds and bats modulate the CPG parameters (frequency, phase difference, and amplitude) for the flapping, twisting, lead-lag, cambering, and flexing of the wings during their flight, as a function of flight speed[3,55,56] and flight modes (e.g., turning, cruising, hovering, preying, and perching). High-speed film analyses[3,55] reveal that the flapping angle and frequency are largest at zero forward speed or in hovering flight, and decrease with increasing flight speed V (e.g., $\propto V^{-0.277}$ for some bats[55]). Such time-varying CPG parameters, shown in Figure 1, will change the shape, size, and flexing of the wings, which constitute the morphological flight parameters.[5] Prior studies in flapping flight, although true in steady flight, assume that there is a constant or very narrow range of optimal frequency or amplitude.[1,2,10–13,16,19,26,28] Tracking a time-varying sinusoidal function with abrupt variations in the frequency and amplitude is a challenge from the perspective of control theory and often requires a high-gain linear control law that is subject to a large initial error. Such large initial errors would lead to violent jerks, actuator saturation, and an unnecessarily large control effort, which could in turn damage the motors and gearboxes[49] (see Figure 3b). In addition, a servo control law, designed from a single frequency of the oscillation, will not be as effective when the original frequency and amplitude need to be modulated (e.g., taking off, perching, turning, or changing speed). In contrast, a CPG model, based on nonlinear limit cycle oscillators like Figures 3a and 3b, can effectively modulate its frequency, amplitude, and convergence rate without affecting its stability. This enhanced smoothness and stability of pattern modulations using coupled limit cycles is essential to the stability of flight dynamics, which might be inherently unstable.

II.A.2. Reduced Dimensionality and Bandwidth Requirement

The CPGs in animal spinal cords are known to relieve the computation burden of locomotion in the brain.[38,47] Similarly, one significant advantage of CPG-based control over conventional control approaches is that *CPG-based control reduces the dimensionality and bandwidth of signals* required from the main controller to its actuators. As shown in Figure 1, the main outer-loop flight controller needs to command only the reduced number of CPG parameters (e.g., frequency, phase lag, and coupling gains) and much less frequently, instead of directly commanding time-specific reference signals for all the degrees of freedom in the wings and the body.

Combining feedback control with model-based reinforcement learning[57] is particularly attractive for control of agile aerospace vehicles, due to the superior robustness and adaptability. Unfortunately, online learning control is subject to the curse of dimensionality, exacerbated by a multitude of joints in the wings. In contrast, the learning-based controller using CPGs needs to adapt only the reduced dimensional CPG parameters. Such a model reduction approach for flight control has not been exploited in the literature. The reduced dimensionality of the CPG-based approach (i.e., controlling the reduced CPG parameters in stead of all relevant degrees of freedom) makes learning-based adaptive flight control more practical.

II.A.3. Symmetric and Symmetry-Breaking Oscillation

Bats have highly complex wing flapping motions that use their multijointed and highly compliant wings, resulting in a closed orbit quite different from a symmetric circle or ellipse of a sinusoidal function. One aim of the neurobiological approach to engineered flapping flight is to produce the analytical model of a wing beat oscillator that matches empirical data.[17,18,55,58] While the benefits of nonlinear limit cycles for CPG models are articulated above, deriving an effective CPG model for engineered flapping flight has been largely an open problem (e.g., limit cycle dynamics, network topology, and how to integrate input and feedback signals). The key research issues include how to ensure the amplitude or phase synchronization of multiple coupled CPG oscillators and how to opportunistically break the symmetry of the oscillators for performing

agile maneuvering of agile flapping flight. Such a flight control method is discussed later in this paper. First, we present how to construct stable coupled oscillators in the next section.

II.B. Global Exponential Synchronization of CPG Oscillators

Synchronization means an exact match of the scaled amplitude or the frequency in this paper. Hence, phase synchronization permits different actuators to oscillate at the same frequency but with some phase lag. However, a sinusoidal function is not adequate to entail the complex coupling and synchronization between various joints and limbs. Hence, the use of coupled nonlinear oscillators in this paper provides a feasible solution to construct complex synchronized motions of multiple wing joints. In essence, each CPG dynamic model in (1) is responsible for generating the limiting oscillatory behavior of a corresponding joint, and the diffusive coupling among CPGs reinforces phase synchronization. For example, the flapping angle has roughly a 90-degree phase difference with the pitching joint to maintain the positive angle of attack (e.g., see the actual data from birds in [3]). The oscillators are connected through diffusive couplings, and the i-th Hopf oscillator can be rewritten with a diffusive coupling with the phase-rotated neighbor.

$$\dot{\mathbf{x}}_i = \mathbf{f}(\mathbf{x}_i; \rho_i) - k \sum_{j \in \mathcal{N}_i}^{m_i} \left(\mathbf{x}_i - \frac{\rho_i}{\rho_j} \mathbf{R}(\Delta_{ij}) \mathbf{x}_j \right) \tag{4}$$

where the Hopf oscillator dynamics $\mathbf{f}(\mathbf{x}_i; \rho_i)$ is defined in (1), $\mathcal{N}_i$ denotes the set that contains only the local neighbors of the i-th Hopf oscillator, and m_i is the number of the neighbors. The 2×2 matrix $\mathbf{R}(\Delta_{ij})$ is a 2-D rotational transformation of the phase difference Δ_{ij} between the i-th and j-th oscillators. The positive (or negative) Δ_{ij} indicates how much phase the i-th member leads (or lags) from the j-th member and $\Delta_{ij} = -\Delta_{ji}$. The positive scalar k denotes the coupling gain.

We construct as many degrees of freedom as needed to more accurately model the joints of the wings, but let us focus on the key three flapping motions defined in Fig. 2, namely flapping angle ϕ_w, wing pitch (twisting) angle θ_w, and wing lead-lag angle ψ_w. Additionally, we assume that there is a second flapping joint ϕ_{w2} in the wing that can reduce the drag in the upstroke by folding the wings toward the body. Then, we can construct the whole state vector of the coupled oscillator such as

$$\{\mathbf{x}\} = \begin{pmatrix} \mathbf{x}_1 \\ \mathbf{x}_2 \\ \mathbf{x}_3 \\ \mathbf{x}_4 \\ \mathbf{x}_5 \\ \mathbf{x}_6 \\ \mathbf{x}_7 \\ \mathbf{x}_8 \end{pmatrix} = \begin{pmatrix} (u_1 - a_1, v_1)^T \\ (u_2 - a_2, v_2)^T \\ (u_3 - a_3, v_3)^T \\ (u_4 - a_4, v_4)^T \\ (u_5 - a_5, v_5)^T \\ (u_6 - a_6, v_6)^T \\ (u_7 - a_7, v_7)^T \\ (u_8 - a_8, v_8)^T \end{pmatrix} = \begin{pmatrix} (\phi_{w_R} - a_1, v_1)^T \\ (\theta_{w_R} - a_2, v_2)^T \\ (\psi_{w_R} - a_3, v_3)^T \\ (\phi_{w2_R} - a_4, v_4)^T \\ (\phi_{w_L} - a_5, v_5)^T \\ (\theta_{w_L} - a_6, v_6)^T \\ (\psi_{w_L} - a_7, v_7)^T \\ (\phi_{w2_L} - a_8, v_8)^T \end{pmatrix} \tag{5}$$

Note that $\mathbf{x}_i$ here might represent the shifted Hopf oscillator vector such that $\mathbf{x}_i = (u_i - a_i, v_i)^T$ as seen in (1), where $a_i(t)$ is the constant or slowly-varying center of oscillation. For example, if we need a 10-degree offset for the main flapping stroke angle ϕ_w, then we can set $a_1 = a_5 = 10$ deg. so that the flapping stroke angle oscillate around 10 degrees.

For stability analysis, we need to construct fully coupled dynamics of the augmented state vector $\{\mathbf{x}\}$.

$$\{\dot{\mathbf{x}}\} = [\mathbf{f}(\{\mathbf{x}\}; \rho)] - k\mathbf{G}\{\mathbf{x}\} \tag{6}$$

where $[\mathbf{f}(\{\mathbf{x}\}; \rho)] = [\mathbf{f}(\mathbf{x}_1; \rho_1); \mathbf{f}(\mathbf{x}_2; \rho_2); \cdots; \mathbf{f}(\mathbf{x}_n; \rho_n)]$. The $2n \times 2n$ matrix $\mathbf{G}$ is a Laplacian matrix with phase shifts $\mathbf{R}(\Delta_{ij})$ constructed from (4).

The coupling topology and phase shift between each oscillators are reflected in the $\mathbf{G}$ matrix. Numerous configurations are possible as long as they are on balanced graphs[59] and we can choose either a bidiretional or a uni-directional coupling between the oscillators. Some configurations considered by the present paper are shown in Fig. 4. The numbers next to the arrows indicate the phase shift Δ_{ij} that the j-th member needs to catch up with the i-th member, hence $\Delta_{ij} > 0$ indicates how much phase the i-th member leads. Since the graphs in Figure 4 are on balanced graphs, the number of input ports equal the number of output

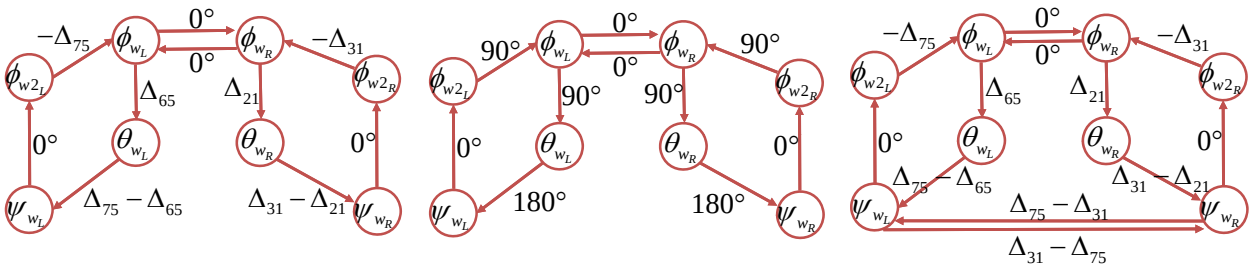

(a) Configuration A (b) Symmetric Configuration A (c) Configuration B

Figure 4. Graph configurations of the coupled Hopf oscillators. Many other configurations are permitted in this paper and the unidirectional couplings can be replaced by the bi-directional couplings. The numbers next to the arrows indicate the phase shift Δ_{ij} from the i-th member to the j-th member while Figure b shows the nominal values of the phase shift from the symmetric wing configuration such that $\Delta_{21} = \Delta_{65}$=90 deg. and $\Delta_{31} = \Delta_{75} = -90$ deg.

ports. Further, all the phase shifts (Δ_{ij}) along one cycle should add up to a modulo of 2π. Figure 4b shows the nominal values of the phase shift from the symmetric wing configuration such that $\Delta_{21} = \Delta_{65} = 90$ deg. and $\Delta_{31} = \Delta_{75} = -90$ deg. The empirical data suggest that the pitching angle (θ_w) has approximately a 90-degree phase lag with the flapping angle (ϕ_w), which agrees with the aerodynamically optimal value.[3,6] For hovering flight, Dickison,[6] using his Robofly testbed and numerical simulations, found that increasing the phase difference value Δ_{21} to 90 deg $+\delta$ further contributed to enhancing the lift generation, which is explained by the wake capture and rotational circulation lift mechanism. Hence, the ability to control Δ_{21} allows us to investigate the optimal value of the phase difference. In addition, the nominal value of $\Delta_{31} = -90$ deg, the phase difference between the flapping stroke angle and lead-lag angle will results an elliptical orbit of the wing. On the other hand, by having two difference phase differences for the left and right wings, we can investigate how symmetric-breaking wing rotations contribute the agile turning of flapping flight. Furthermore, by having an independent control of the phase difference Δ_{31} and Δ_{75}, we can investigate another symmetry-breaking impact of the differential delay in the lead-lag motion. Such differential phases are used to stabilize the flapping flying dynamics in Section IV.

The $\mathbf{G}$ matrix in (6) for Fig. 4a can be found as $\mathbf{G} =$

$$\begin{bmatrix}
2\mathbf{I}_2 & \mathbf{0} & \mathbf{0} & \frac{\rho_1}{\rho_4}\mathbf{R}(\Delta_{31}) & -\frac{\rho_1}{\rho_5}\mathbf{I}_2 & \mathbf{0} & \mathbf{0} & \mathbf{0} \\
-\frac{\rho_2}{\rho_1}\mathbf{R}(\Delta_{21}) & \mathbf{I}_2 & \mathbf{0} & \mathbf{0} & \mathbf{0} & \mathbf{0} & \mathbf{0} & \mathbf{0} \\
\mathbf{0} & -\frac{\rho_3}{\rho_2}\mathbf{R}(\Delta_{31}-\Delta_{21}) & \mathbf{I}_2 & \mathbf{0} & \mathbf{0} & \mathbf{0} & \mathbf{0} & \mathbf{0} \\
\mathbf{0} & \mathbf{0} & -\frac{\rho_4}{\rho_3}\mathbf{I}_2 & \mathbf{I}_2 & \mathbf{0} & \mathbf{0} & \mathbf{0} & \mathbf{0} \\
-\frac{\rho_5}{\rho_1}\mathbf{I}_2 & \mathbf{0} & \mathbf{0} & \mathbf{0} & 2\mathbf{I}_2 & \mathbf{0} & \mathbf{0} & \frac{\rho_5}{\rho_8}\mathbf{R}(\Delta_{75}) \\
\mathbf{0} & \mathbf{0} & \mathbf{0} & \mathbf{0} & -\frac{\rho_6}{\rho_5}\mathbf{R}(\Delta_{65}) & \mathbf{I}_2 & \mathbf{0} & \mathbf{0} \\
\mathbf{0} & \mathbf{0} & \mathbf{0} & \mathbf{0} & \mathbf{0} & -\frac{\rho_7}{\rho_6}\mathbf{R}(\Delta_{75}-\Delta_{65}) & \mathbf{I}_2 & \mathbf{0} \\
\mathbf{0} & \mathbf{0} & \mathbf{0} & \mathbf{0} & \mathbf{0} & \mathbf{0} & -\frac{\rho_8}{\rho_7}\mathbf{I}_2 & \mathbf{I}_2
\end{bmatrix} \tag{7}$$

where in general, the radii (the amplitude of the oscillation from the bias a_i) are symmetric such that $\rho_1 = \rho_2$, $\rho_2 = \rho_6$, $\rho_4 = \rho_7$, and $\rho_5 = \rho_8$, although the difference of the maximum amplitude of each oscillation can occasionally be used to generate side forces or turning (rolling or yawing) moments.

The proof of phase synchronization boils down to finding the condition of k by which the flow-invariant synchronized state,[53] constructed from $\mathbf{G}\{\mathbf{x}\} = \mathbf{0}$, is globally stable. In fact, by using contraction theory,[53,60] we can prove global exponential synchronization of the coupled Hopf oscillators. We first introduce the main theorem of contraction theory

Theorem 1 *For the system $\dot{\mathbf{x}} = \mathbf{f}(\mathbf{x}, t)$, if there exists a uniformly positive definite metric, $\mathbf{M}(\mathbf{x}, t) = \mathbf{\Theta}(\mathbf{x}, t)^T\mathbf{\Theta}(\mathbf{x}, t)$, where $\mathbf{\Theta}$ is some smooth coordinate transformation of the virtual displacement, $\delta\mathbf{z} = \mathbf{\Theta}\delta\mathbf{x}$, such that the associated generalized Jacobian, F is uniformly negative definite, i.e., $\exists \ell > 0$ such that*

$$\mathbf{F} = \left(\dot{\mathbf{\Theta}}(\mathbf{x}, t) + \mathbf{\Theta}(\mathbf{x}, t)\frac{\partial \mathbf{f}}{\partial \mathbf{x}}\right)\mathbf{\Theta}(\mathbf{x}, t)^{-1} \leq -\ell\mathbf{I}, \tag{8}$$

then all system trajectories converge globally to a single trajectory exponentially fast regardless of the initial conditions, with a global exponential convergence rate of the largest eigenvalues of the symmetric part of $\mathbf{F}$.

Such a system is said to be contracting.

Proof 1 *The proof is given in [60] by computing* $\frac{d}{dt}\delta\mathbf{z}^T\delta\mathbf{z} = 2\delta\mathbf{z}^T\mathbf{F}\delta\mathbf{z}$. □

The synchronized flow-invariant subspace for the configuration in Fig 4a is defined by $\mathbf{G}\{\mathbf{x}\} = \mathbf{0}$ such that

$$\begin{aligned}\mathcal{M}(\{\mathbf{x}\}) \Longleftrightarrow & \mathbf{x}_1 = \frac{\rho_1}{\rho_2}\mathbf{R}(\Delta_{12})\mathbf{x}_2 = \frac{\rho_1}{\rho_3}\mathbf{R}(\Delta_{13})\mathbf{x}_3 = \frac{\rho_1}{\rho_4}\mathbf{R}(\Delta_{13})\mathbf{x}_4 \\ = & \frac{\rho_1}{\rho_5}\mathbf{x}_5 = \frac{\rho_1}{\rho_6}\mathbf{R}(\Delta_{56})\mathbf{x}_6 = \frac{\rho_1}{\rho_7}\mathbf{R}(\Delta_{57})\mathbf{x}_7 = \frac{\rho_1}{\rho_8}\mathbf{R}(\Delta_{57})\mathbf{x}_8 \end{aligned} \tag{9}$$

where we used $\Delta_{ij} = -\Delta_{ji}$.

The flow invariant subspace $\mathcal{M}$ in (9) can be re-written with respect to the first state vector $\mathbf{x}_1 = \mathbf{z}_1$ such that

$$\mathcal{M}(\{\mathbf{x}\}) \Longleftrightarrow \mathbf{z}_1 = \mathbf{z}_2 = \cdots = \mathbf{z}_n, \quad \{\mathbf{z}\} = \mathbf{T}(\Delta_{ij}, \rho_i)\{\mathbf{x}\} \tag{10}$$

where $\{\mathbf{z}\} = (\mathbf{z}_1, \mathbf{z}_2, \cdots, \mathbf{z}_n)^T$ and $\mathbf{z}_1 = \mathbf{x}_1$, $\mathbf{z}_2 = \frac{\rho_1}{\rho_2}\mathbf{R}(\Delta_{12})\mathbf{x}_2$, $\mathbf{z}_3 = \frac{\rho_1}{\rho_3}\mathbf{R}(\Delta_{13})\mathbf{x}_3$ and so on. For example, the $\mathbf{T}$ matrix for the configuration in Fig. 4a is given as

$$\mathbf{T}(\Delta_{ij}, \rho_i) = \text{diag}\left(\mathbf{I}_2, \frac{\rho_1}{\rho_2}\mathbf{R}(\Delta_{12}), \frac{\rho_1}{\rho_3}\mathbf{R}(\Delta_{13}), \frac{\rho_1}{\rho_4}\mathbf{R}(\Delta_{13}), \frac{\rho_1}{\rho_5}\mathbf{I}_2, \frac{\rho_1}{\rho_6}\mathbf{R}(\Delta_{56}), \frac{\rho_1}{\rho_7}\mathbf{R}(\Delta_{57}), \frac{\rho_1}{\rho_8}\mathbf{R}(\Delta_{57})\right) \tag{11}$$

Then, we present the main theorem of this section.

Theorem 2 *If the following condition is met, any initial condition* $\{\mathbf{x}\}$ *of the coupled Hopf oscillators in (4) and (6) on a balanced graph converges to the flow-invariant synchronized state* $\mathcal{M}$ *exponentially fast.*

$$k\lambda_{min}\left(\mathbf{V}^T(\mathbf{L} + \mathbf{L}^T)\mathbf{V}/2\right) > \lambda \tag{12}$$

where λ *is the convergence rate of the Hopf oscillator in (1),* $\lambda_{min}\left(\mathbf{V}^T(\mathbf{L} + \mathbf{L}^T)\mathbf{V}/2\right)$ *denotes the minimum eigenvalue, and* $\mathbf{L}$ *is the Laplacian matrix constructed from the balanced graph such that* $\mathbf{G} = \mathbf{T}^{-1}\mathbf{L}\mathbf{T}$ *with* $\mathbf{T}$ *defined from (10). In addition, the real orthonormal* $2n \times 2(n-1)$ *matrix* $\mathbf{V}$ *is constructed from the orthonormal eigenvectors of* $(\mathbf{L} + \mathbf{L}^T)/2$ *other than the ones vector* $\mathbf{1} = (\mathbf{I}_2; \mathbf{I}_2; \cdots; \mathbf{I}_2)$ *such that* $\mathbf{V}\mathbf{V}^T + \mathbf{1}\mathbf{1}^T/n = \mathbf{I}_{2n}$.

Proof 2 *The proof can be obtained based on [53]. Consider the orthonormal space* $\mathbf{V}$*, constructed from the orthornomal eigenvectors of the symmetric part of* $\mathbf{L}$ *(e.g. see [59]). Then, the global exponential convergence to the flow-invariant synchronized state* $\mathcal{M}$ *is equivalent to*

$$\mathbf{V}^T\{\mathbf{z}\} \to 0, \quad \textit{globally and exponentially} \tag{13}$$

By pre-multiplying (6) by $\mathbf{T}^{-1}$ *and using* $\mathbf{T}\{\mathbf{x}\} = \{\mathbf{z}\}$ *and* $\mathbf{G} = \mathbf{T}^{-1}\mathbf{L}\mathbf{T}$*, we can obtain*

$$\{\dot{\mathbf{z}}\} = \mathbf{T}\left[\mathbf{f}(\{\mathbf{x}\}; \rho)\right] - k\mathbf{L}\{\mathbf{z}\} \tag{14}$$

where for the example in Fig. 4a we can verify

$$\mathbf{L} = \begin{bmatrix} 2\mathbf{I}_2 & \mathbf{0} & \mathbf{0} & -\mathbf{I}_2 & -\mathbf{I}_2 & \mathbf{0} & \mathbf{0} & \mathbf{0} \\ -\mathbf{I}_2 & \mathbf{I}_2 & \mathbf{0} & \mathbf{0} & \mathbf{0} & \mathbf{0} & \mathbf{0} & \mathbf{0} \\ \mathbf{0} & -\mathbf{I}_2 & \mathbf{I}_2 & \mathbf{0} & \mathbf{0} & \mathbf{0} & \mathbf{0} & \mathbf{0} \\ \mathbf{0} & \mathbf{0} & -\mathbf{I}_2 & \mathbf{I}_2 & \mathbf{0} & \mathbf{0} & \mathbf{0} & \mathbf{0} \\ -\mathbf{I}_2 & \mathbf{0} & \mathbf{0} & \mathbf{0} & 2\mathbf{I}_2 & \mathbf{0} & \mathbf{0} & -\mathbf{I}_2 \\ \mathbf{0} & \mathbf{0} & \mathbf{0} & \mathbf{0} & -\mathbf{I}_2 & \mathbf{I}_2 & \mathbf{0} & \mathbf{0} \\ \mathbf{0} & \mathbf{0} & \mathbf{0} & \mathbf{0} & \mathbf{0} & -\mathbf{I}_2 & \mathbf{I}_2 & \mathbf{0} \\ \mathbf{0} & \mathbf{0} & \mathbf{0} & \mathbf{0} & \mathbf{0} & \mathbf{0} & -\mathbf{I}_2 & \mathbf{I}_2 \end{bmatrix} \tag{15}$$

In other words, we transformed the $\mathbf{G}$ *matrix to the conventional graph Laplacian matrix* $\mathbf{L}$.

Since $\mathbf{T}\left[\mathbf{f}(\{\mathbf{x}\};\rho)\right] = \mathbf{T}\left[\mathbf{f}(\mathbf{T}^{-1}\{\mathbf{z}\};\rho)\right]$, *we can find*

$$\begin{aligned}\mathbf{T}\left[\mathbf{f}(\{\mathbf{x}\};\rho)\right] &= \left[\frac{\rho_1}{\rho_i}\mathbf{R}(-\Delta_{1j})\mathbf{f}(\mathbf{x}_i;\rho_i)\right] = \left[\frac{\rho_1}{\rho_i}\mathbf{R}(-\Delta_{1j})\mathbf{f}(\frac{\rho_i}{\rho_1}\mathbf{R}(\Delta_{1j})\mathbf{z}_i;\rho_i)\right] \\ &= \left[\mathbf{f}(\mathbf{z}_i;\rho_1)\right] = \left[\mathbf{f}(\mathbf{z}_1;\rho_1);\mathbf{f}(\mathbf{z}_2;\rho_1);\cdots;\mathbf{f}(\mathbf{z}_n;\rho_1)\right]\end{aligned} \tag{16}$$

where we used $\mathbf{f}(\mathbf{R}(\Delta)\mathbf{x}) = \mathbf{R}(\Delta)\mathbf{f}(\mathbf{x})$ *and* $\mathbf{f}(g\mathbf{x};\rho) = g\mathbf{f}(\mathbf{x};\rho/g)$ *from (2) and (3). Note that the radius of the final augmented Hopf oscillators in (16) is identical to* ρ_1.

By premultiplying $\boldsymbol{V}^T$ *and substituting* $\{\mathbf{z}\} = \mathbf{V}\mathbf{V}^T\{\mathbf{z}\} + \mathbf{1}\mathbf{1}^T\{\mathbf{z}\}$ *result in*

$$\mathbf{V}^T\{\dot{\mathbf{z}}\} = \mathbf{V}^T\left[\mathbf{f}(\mathbf{V}\mathbf{V}^T\{\mathbf{z}\} + \mathbf{1}\mathbf{1}^T/n\{\mathbf{z}\};\rho_1)\right] - k\mathbf{V}^T\mathbf{L}\mathbf{V}\mathbf{V}^T\{\mathbf{z}\} \tag{17}$$

where we used $\mathbf{L}\mathbf{1}\mathbf{1}^T = 0$.

We can construct the following virtual dynamics of $\mathbf{y}$ *from the preceding equation*

$$\dot{\mathbf{y}} = \mathbf{V}^T\left[\mathbf{f}(\mathbf{V}\mathbf{y} + \mathbf{1}\mathbf{1}^T/n\{\mathbf{z}\};\rho_1)\right] - k\mathbf{V}^T\mathbf{L}\mathbf{V}\mathbf{y} \tag{18}$$

which has $\mathbf{y} = \mathbf{V}^T\{\mathbf{z}\}$ *and* $\mathbf{y} = \mathbf{0}$ *has two particular solutions.*

The virtual system (18) is contracting (globally and exponentially stable) for $\mathbf{V}^T\left[\mathbf{f}\right]\mathbf{V} - k\mathbf{V}^T(\mathbf{L}+\mathbf{L}^T)\mathbf{V}/2 < 0$ *by Theorem 1. This condition is equivalent to* $k\lambda_{min}\left(\mathbf{V}^T(\mathbf{L}+\mathbf{L}^T)\mathbf{V}/2\right) > \lambda$, *since the maximum eigenvalue of* $\lambda_{max}(\mathbf{V}^T\left[\mathbf{f}\right]\mathbf{V}) \leq \lambda$. *For the example in Fig. 4a, this condition corresponds to* $k > \lambda/0.198$.

The same proof works for an arbitrary CPG network on balanced graph that has $\mathbf{V}^T(\mathbf{L}+\mathbf{L}^T)\mathbf{V}/2 > 0$. *For undirected graphs (all the connections are bi-directional),* $\mathbf{L}$ *automatically becomes a balanced symmetric matrix.* □

In conclusion, Theorem 2 can be used to find the proper coupling strength k to exponentially and globally stabilize the coupled Hopf oscillators given in (4). Sometimes, the condition for k in Theorem 2 might be too conservative especially if the desired λ is large. In fact, for any positive coupling gain $k > 0$, it is shown that coupled Hopf oscillators globally synchronize[54] although the convergence results become asymptotic not exponential.

II.C. Perspectives on Sensory Feedback Connection

The property of robustness, inherent in the CPG-based control, is particularly emphasized by the literature (see [61]). Stable locomotion can be achieved using the interaction between the CPG model, the physical model of the body, and the environment.[62] Most models[40,49,63] use an open-loop approach without sensor feedback, while some others[56,64] incorporate sensor feedback to modulate the reference oscillator patterns. One drawback is that such open-loop approaches do not ensure the synchronization of the physical states in the presence of external disturbances. In other words, the mutual entrainment[47,62,65] between the CPG and the mechanical body is not guaranteed. Recently, a new CPG-based method that reinforces emerging rhythmic patterns of actual physical joints like foil-fin actuators has been proposed.[46] Such a reflex-based closed-loop CPG method, although currently applied only to a simpler and more stable swimming robot, has a potential for discovering practical ways of flapping wing coordination in the presence of external disturbances, even without using a reference oscillator. In this paper, we show how to use local motor control feedback and vehicle states such as the attitude and velocity vectors can be used to adapt the CPG oscillation parameters.

In the next section, we present the wing kinematic model and the dynamic model of flapping flight dynamics that can be driven by the CPG network.

III. Wing Kinematics, Aerodynamic Forces, and Vehicle Dynamics

We first derive a simplified wing kinematic model of a flapping wing blade element in Section III.A before presenting the complex three dimensional model in Section III.B. Based on the forces and torques from the three-dimensional wing kinematics, we present the 6-DOF dynamic equations of motion of flapping flight that can be used to validate the coupled wing control driven by CPG in Section III.C.

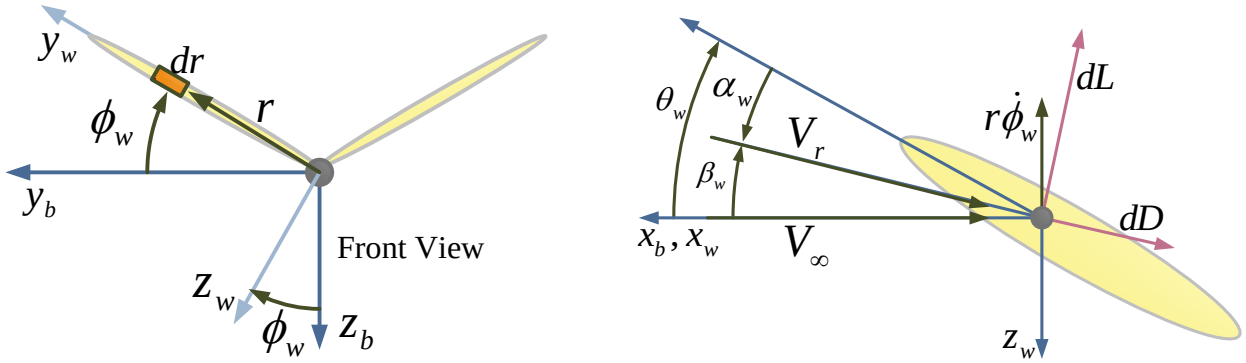

(a) Front view of the body.

(b) Cross-sectional view of a wing blade element dr in the stroke plane

Figure 5. Schematic of a simplified model

III.A. Simplified Wing Kinematic Models

The simplified wing kinematic model supports both flexible and rigid wings. The aim of this section is to illustrate that the effective angle of attack varies as a function of the wing span distance as well as the flapping (stroke) angular rate and it can be effectively controlled by the synchronized pitching (wing rotation) control. This simple model sheds light on some essential mechanisms of biological flapping flight. We assume that the flapping flying vehicle is flying horizontally with a zero flight path angle and 90-deg stroke plane angle as shown Figure 5. We also ignore at the moment the induced flow of the wind. Throughout this paper, the positive direction of the stroke angle ϕ_w is the upstroke direction for both right and left wings, hence a negative rotation about the x-axis yields a positive stroke angle for the right wing (see Fig. 5(a)). The body axes coordinates are (x_b, y_b, z_b), and the wing frame (x_w, y_w, z_w) is rotated by the instantaneous stroke angle ϕ_w. Hence, the rotated wing frame axes y_w and z_w define the wing stroke plane.

In order to compute the local effective angle of attack α_w of the blade element dr along the wing span, we find the direction of the local relative wind V_r, as shown in Fig. 5(b). The direction of the local relative wind β_w due to the combined wing stroke motion (ϕ_w) and forward speed V_∞ can be obtained and expressed in terms of the reduced frequency k_r of the flapping wing:

$$\beta_w(r,t) = \tan^{-1}\frac{r\dot{\phi}_w}{V_\infty} = \tan^{-1}\frac{2rk_r}{c} \quad \text{and } k_r = \frac{\dot{\phi}_w c}{2V_\infty} \tag{19}$$

where r is the wing span coordinate $r \in [0, R]$ with R is the wing span of a single wing, and $c(r)$ is the wing chord as a function of r. Also, note that the β_w is measured from the body x-axis clockwise. The reduced frequency k compares the velocity by the wing flapping motion with the forward speed, thereby indicating the degree of unsteady aerodynamics. Note that some prefer to use the Strouhal number (st) or the advance ratio $J = V_\infty/(2\phi_{max} fR)$ with the flapping frequency f and the total wing span R.[2,9,16]
Note that the sign of β_w is consistent with the positive direction of the flapping (stroke) angle ϕ_w since the downstroke $\dot{\phi}_w < 0$ leads to the negative flow angle $\beta_w < 0$. The local angle of attack of the blade element at r with the width dr becomes

$$\alpha_w(r,t) = \theta_w(t) - \beta_w(r,t) \tag{20}$$

where $\theta_w(t)$, measured from the body x-axis, is a pitch angle of the wing driven by the CPG oscillator in (1) and (4). The positive direction of $\theta_w(t)$ is clockwise (pitch-up) and called supination, whereas the negative pitch is called pronation.

Equation 20 correctly predicts that the lift and thrust forces are larger at the outer wing, since the β_w angle in downstroke is more negative as r increases toward the wing tip, while the local angle of attack $\alpha_w(r)$ increases as well. This also suggests a control logic for the wing pitch rotation $\theta_w(t)$ to main the positive angle of attack for time-varying $\beta_w(t)$.

Once we obtain the function of the local effective angle of attack, we can proceed to obtain the aerodynamic forces of the blade element by evaluating the lift and drag coefficients, $C_L(\alpha)$ and $C_D(\alpha)$. Flapping flight, typically within a low Reynolds number regime ($\text{Re} < 10^5$), is governed by unsteady aerodynamics characterized by large-scale vortex structures. It is understood that the main lift enhancement mechanism

of flapping flight is governed by (1) the leading edge vortex (LEV) that leads to delayed stall at a very high angle of attack, (2) the rotational circulation lift, and (3) wake capture that generate aerodynamic forces during flapping angle reversals.[6] In particular, Dickinson's series of papers,[6,9] by cross-validating the numerical computation and experimentation using the Robofly, shows that a quasi-steady aerodynamic model predicts the aerodynamic coefficients reasonably well. CFD methods that would require numerous hours and days of computation for more accurate unsteady aerodynamics are not suited for a control design, especially when such modeling errors can be addressed by robust control. Further, this quasi-steady approximation method can be verified and improved by the experimental set-up described in Section V.

The seminal paper by Dickison,[6] used a hovering pair of wings without a forward speed as follows

$$\begin{aligned} C_L(\alpha_w) &= 0.225 + 1.58\sin(2.13\alpha_w - 7.2\,\text{deg}) \\ C_D(\alpha_w) &= 1.92 - 1.55\cos(2.04\alpha_w - 9.82\,\text{deg}) \end{aligned} \tag{21}$$

It should be noted that Dickinson's robotfly's setup used a horizontal stroke plane, as typically seen in insect flight, whereas we assume a 90-deg stroke plane angle. Note that the angle α_w for a general flapping wing is time-varying, as described in this section. Also, a recent paper[9] that considers a nonzero-forward speed. These aerodynamic coefficients become functions of the reduced frequency (k_r) with a non-zero forward speed:

$$C_L(\alpha_w) = K_{l1}(k_r)\sin\alpha_w\cos\alpha_w \tag{22}$$

$$C_D(\alpha_w) = K_{d1}(k_r)\sin^2\alpha_w + K_{d0}(k_r), \qquad k_r = \frac{\dot{\phi}_{w,max}c}{2V_\infty} \tag{23}$$

where we modified the definition of the reduced frequency k_r slightly with a constant maximum stroke angular rate $\dot{\phi}_{w,max}$, since $\dot{\phi}_w$ in (19) is time-varying. The experimental setup introduced in this paper allows us to measure such coefficients.

From the quasi-steady approximation of C_L and C_D, we can compute the lift and drag forces acting on the blade element with the width dr as follows.

$$\begin{aligned} dL &= \frac{1}{2}\rho C_L\left(\alpha_w(r,t)\right)c(r)V_r^2(r,t)dr \\ dD &= \frac{1}{2}\rho C_D\left(\alpha_w(r,t)\right)c(r)V_r^2(r,t)dr \end{aligned} \tag{24}$$

where $V_r(r,t) = \sqrt{(r\dot{\phi})^2 + V_\infty^2}$ and

In addition, Ellington[10] derived the wing circulation $\Gamma_r = \pi\dot{\alpha}c^2(3/4 - \hat{x}_0)$ based on the Kutta-Joukowski condition. This quasi-steady approximation for the rotational lift can be written as

$$dL_{rot} = \frac{1}{2}\rho\left(2\pi(\frac{3}{4} - \hat{x}_0)\right)c^2(r)V_r(r,t)\dot{\alpha}_w dr \tag{25}$$

where $\hat{x}_0$ is the location of the pitch axis along the mean chord length. Also, $\dot{\alpha}_w$ can be computed from (20) and often approximated reasonably well by the angular rate of the wing pitch motion $\dot{\theta}_w$.

The total x and z directional forces of a single wing (either right or left) in the body frame are obtained as

$$\begin{aligned} F_{wz} &= \int_{r=0}^{R} dD\sin\beta_w - (dL + dL_{rot})\cos\beta_w \\ F_{wx} &= \int_{r=0}^{R} -(dL + dL_{rot})\sin\beta_w - dD\cos\beta_w \end{aligned} \tag{26}$$

Note that the positive direction of z_b is downward as shown in Fig. 5.

III.B. Three-Dimensional Wing Kinematics and Aerodynamic Forces

We present a more realistic modeling that encompasses a tilted stroke angle, the lead-lag motion, and the relative body velocity, in addition to the stroke and pitch angles. In deriving these equations, the actual

control degrees-of-freedom of the robotic bat MAV testbed, which is presented in Section V, are considered. Figure 6a shows a side view of the flapping flying MAV with the body frame $\mathbf{x}_b = (x_b, y_b, z_b)^T$ and the stroke-plane frame $\mathbf{x}_s = (x_s, y_s, z_s)^T$ of the right wing. In this section, we present only the equations of the right wing since the similar expressions for the left wing can straightforwardly follow. The center of the stroke-plane frame is located at (d_x, d_y, d_z), and it is tilted by the inclination angle $\Theta_s(t)$, which can be a function of time and the forward velocity. Without the lead-lag motion, the axes y_s and z_s define the stroke plane. Hence, the transformation between these coordinate axes can be given by

$$\mathbf{x}_b = \mathbf{T}_{bs}(\Theta_s)\mathbf{x}_s + (d_x, d_y, d_z)^T, \quad \text{where} \quad \mathbf{T}_{bs}(\Theta_s) = \begin{bmatrix} \cos\Theta_s & 0 & \sin\Theta_s \\ 0 & 1 & 0 \\ -\sin\Theta_s & 0 & \cos\Theta_s \end{bmatrix} \tag{27}$$

where in this paper $\mathbf{T}_{bs}$ denotes the transformation from $\mathbf{x}_s$ to $\mathbf{x}_b$, whereas $\mathbf{T}_{sb} = \mathbf{T}_{bs}^T$ would correspond to the transformation from $\mathbf{x}_b$ to $\mathbf{x}_s$.
For a hovering insect, the stroke plane is almost horizontal (i.e., $\Theta_s = 90$ deg in our coordinate definition in Fig 6a), resulting in forward and backward reciprocating motions. This is the assumption used for some prior work.[6,9,19,20] In contrast, the stroke angle of birds and bats varies as a function of flight speed; at a low speed, the angle is almost horizontal ($\Theta_s = 90$ deg) and it approaches $\Theta_s = 0$ deg as the flight speed increases.

If there is no lead-lag motion, the additional transformation for a wing stroke angle ϕ_w, similar to Fig. 5b, would complete all the required transformation between the body frame and the wing frame. However, a nonzero lead-lag angle further complicates the wing kinematics. Choosing the rotational axes for flapping, lead-lag, and pitch depends on the actual hardware setup and actuators, and our choice is influenced by the robotic bat MAV presented in this paper. In contrast with Azuma's derivation in [3] where the stroke angle $\Theta_s(t)$ is dependent on the $\phi_w(t)$ and the lead-lag angle $\psi_w(t)$, our $\Theta_s(t)$ is an independent control variable. Our decision is based on the observation that $\Theta_s(t)$ can be an important control variable for efficient engineered flapping flight. Further, this kind of actuator mechanism is easier to implement and control. As shown in Fig. 6b, the lead-lag angle is defined by the rotation about the z_s axis- the z-axis in the stroke plane frame. In contrast with the fixed angle rotation in [3], then we rotate about the new x-axis to obtain the wing frame $\mathbf{x}_w$. The positive direction of ψ_w is the forward direction, while the positive stroke angle ϕ_w indicates an upstroke motion. This sign convention does not agree with the original positive direction of rotation for the right wing, so extra care should be taken to determine the correct angular transformation matrices.

For the right wing, the transformation between the stroke plane frame ($\mathbf{x}_s$) and the wing frame ($\mathbf{x}_w$) can be written as

$$\begin{aligned} \mathbf{x}_s = \mathbf{T}_{sw}(\phi_w, \psi_w)\mathbf{x}_w &= \begin{bmatrix} \cos\psi_w & \sin\psi_w & 0 \\ -\sin\psi_w & \cos\psi_w & 0 \\ 0 & 0 & 1 \end{bmatrix} \begin{bmatrix} 1 & 0 & 0 \\ 0 & \cos\phi_w & \sin\phi_w \\ 0 & -\sin\phi_w & \cos\phi_w \end{bmatrix} \mathbf{x}_w \\ &= \begin{bmatrix} \cos\psi_w & \cos\phi_w\sin\psi_w & \sin\phi_w\sin\psi_w \\ -\sin\psi_w & \cos\phi_w\cos\psi_w & \sin_w\,\phi_w\cos\psi_w \\ 0 & -\sin\phi_w & \cos\phi_w \end{bmatrix} \mathbf{x}_w \end{aligned} \tag{28}$$

In order to compute the local lift and drag of a blade element, we need to transform the velocities in body coordinates to the incident velocities in the rotated wing frame. For example, consider the free-stream forward speed V_∞ with the body angle of attack α_x and the side-slip angle α_y. Note that α_y is commonly denoted by β in the aerospace community, but in this paper β denotes the direction of the relative wind of a blade element. Then, the free-stream velocity in the body frame can be written as

$$\mathbf{V}_b = (V_\infty \cos\alpha_y \cos\alpha_x, V_\infty \sin\alpha_y, V_\infty \cos\alpha_y \sin\alpha_x)^T + \mathbf{v}_i + \mathbf{v}_E \tag{29}$$

where $\mathbf{v}_i$ and $\mathbf{v}_E$ denote the induced velocity vector and the wind velocity vector respectively. In other words, in the absence of $\mathbf{v}_i$ and $\mathbf{v}_E$, the vector $\mathbf{V}_b$ equals the velocity of the vehicle in the body frame. Let us assume that α_x and α_y include the effects of the induced velocity and $\mathbf{v}_E$ is small.

Then, the free-velocity vector $\mathbf{V}_b$ in the body frame can be transformed to the wind frame. In addition, we can also compute the additional velocity on the wing frame induced from the body angular rate $\mathbf{\Omega}_b = (p, q, r)^T$

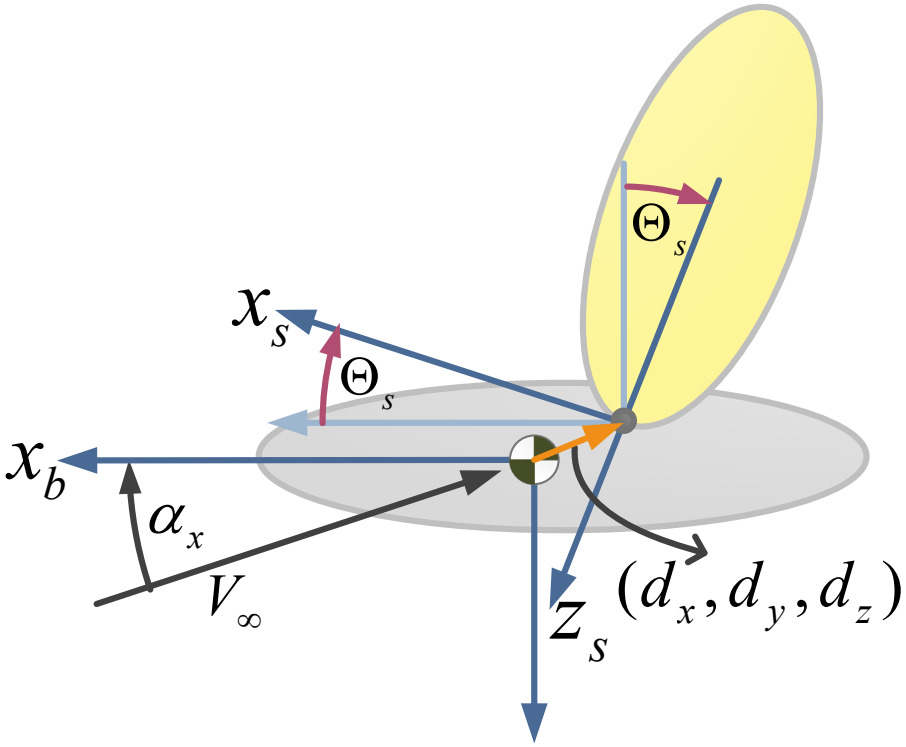

(a) Transformation from the body frame to the stroke plane frame

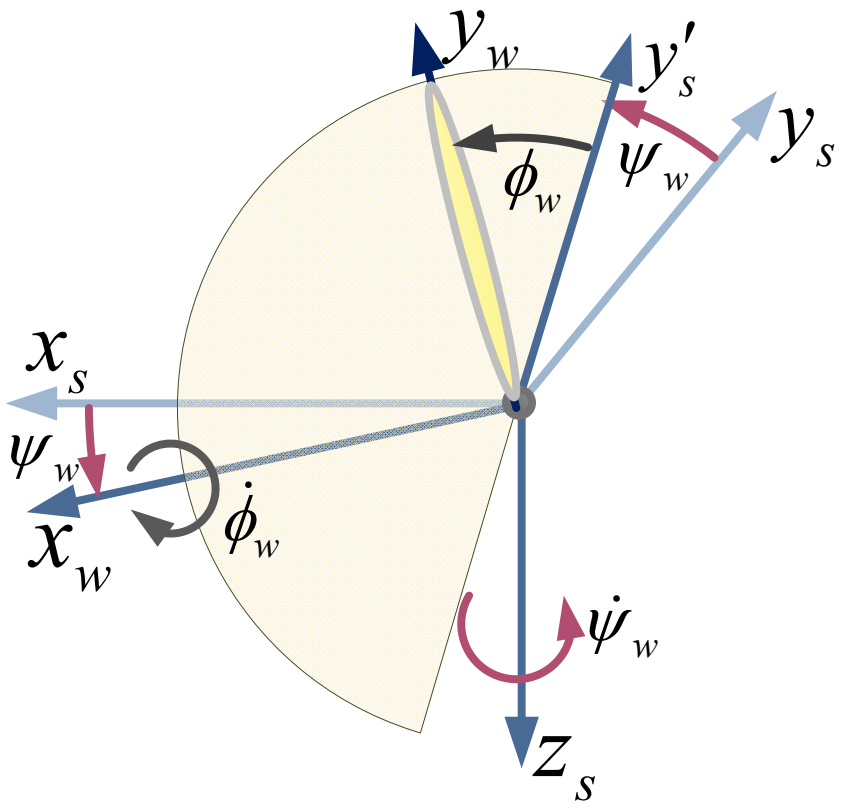

(b) Transformation from the stroke plane frame to the wing frame

Figure 6. Schematic of the 3D wing motions

and the offset distance $\mathbf{d} = (d_x, d_y, d_z)^T$ of the stroke plane frame (see Fig. 6a). By adding these two terms, we can obtain

$$\mathbf{V}_b^w = \mathbf{T}_{ws}(\phi_w, \psi_w)\mathbf{T}_{sb}(\Theta_s)(\mathbf{V}_b + \mathbf{\Omega}_b \times \mathbf{d}) \tag{30}$$

In order to compute the rotational velocity on the wing frame produced by the flapping ϕ_w and lead-lag ψ_w motions, as well as a relatively slower stroke angle change $\Theta_s(t)$, it is more convenient to construct the angular rate vector in the stroke plane frame as follows

$$\mathbf{\Omega}_{tot} = \mathbf{T}_{sb}(\Theta_s)\mathbf{\Omega}_b + \begin{pmatrix} -\cos\psi_w\dot{\phi}_w \\ \sin\psi_w\dot{\phi}_w + \dot{\Theta}_s \\ -\dot{\psi}_w \end{pmatrix} \tag{31}$$

Then, we can compute the induced rotational velocity from the wing motions of the blade element dr

$$\mathbf{V}_{rot}^w = (\mathbf{T}_{ws}(\phi_w, \psi_w)\mathbf{\Omega}_{tot}) \times \left(\begin{pmatrix} 0 \\ r \\ 0 \end{pmatrix} + \begin{pmatrix} x_w(r) \\ y_w(r) \\ z_w(r) \end{pmatrix} \right) + \begin{pmatrix} \dot{x}_w(r) \\ \dot{y}_w(r) \\ \dot{z}_w(r) \end{pmatrix} \tag{32}$$

where $x_w(r)$, $y_w(r)$ and $z_w(r)$ are the deformation of the blade element due to aeroelastic deformation or active cambering control that can be found in bat flight. Hence, the derivations in this section can be used for flexible wing models, although the $C_L(\alpha)$ and $C_D(\alpha)$ functions should be corrected for such camberred wing shapes.

By adding $\mathbf{V}_b^w$ in (30) and $\mathbf{V}_{rot}^w$ in (32), we can obtain the total velocity of the wind at the blade element, distanced from r on the wing span axis, as follows

$$\mathbf{V}_w = \begin{pmatrix} V_{wx} \\ V_{wy} \\ V_{wz} \end{pmatrix} = \mathbf{T}_{ws}(\phi_w, \psi_w)\mathbf{T}_{sb}(\Theta_s)(\mathbf{V}_b + \mathbf{\Omega}_b \times \mathbf{d}) + (\mathbf{T}_{ws}(\phi_w, \psi_w)\mathbf{\Omega}_{tot}) \times \left(\begin{pmatrix} 0 \\ r \\ 0 \end{pmatrix} + \begin{pmatrix} x_w(r) \\ y_w(r) \\ z_w(r) \end{pmatrix} \right) + \begin{pmatrix} \dot{x}_w(r) \\ \dot{y}_w(r) \\ \dot{z}_w(r) \end{pmatrix} \tag{33}$$

A similar expressions can be obtained for the left wing.

Now, we can obtain the local effective angle of attack α_w of the blade element to determine aerodynamic forces and torque. Let us assume that the deformation of a rigid wing is negligible and there is no active cambering control. Also, the contribution from the body angular rate $\mathbf{\Omega}_b$ is small. Then, (33) reduces to

$$\begin{pmatrix} V_{wx} \\ V_{wy} \\ V_{wz} \end{pmatrix} = \mathbf{T}_{ws}(\phi_w, \psi_w)\mathbf{T}_{sb}(\Theta_s)\mathbf{V}_b + \left(\mathbf{T}_{ws}(\phi_w, \psi_w) \begin{pmatrix} -\cos\psi_w\dot{\phi}_w \\ \sin\psi_w\dot{\phi}_w + \dot{\Theta}_s \\ -\dot{\psi}_w \end{pmatrix} \right) \times \begin{pmatrix} 0 \\ r \\ 0 \end{pmatrix} \tag{34}$$

$$= \begin{pmatrix} V_\infty \cos\psi_w \cos(\Theta_s + \alpha_x)\cos\alpha_y - V_\infty \sin\psi_w \sin\alpha_y - r\cos\psi_w \sin\phi_w\dot{\Theta}_s + r\cos\phi_w\dot{\psi}_w \\ V_\infty \cos\alpha_y \left(\cos\phi_w \cos(\Theta_s + \alpha_x)\sin\psi_w - \sin\phi_w \sin(\Theta_s + \alpha_x)\right) + V_\infty \cos\phi_w \cos\psi_w \sin\alpha_y \\ V_\infty \cos\alpha_y \left(\cos(\Theta_s + \alpha_x)\sin\phi_w \sin\psi_w + \cos\phi_w \sin(\Theta_s + \alpha_x)\right) + V_\infty \cos\psi_w \sin\phi_w \sin\alpha_y - r(\sin\psi_w\dot{\Theta}_s + \dot{\phi}_w) \end{pmatrix}$$

Then, similar to (19), we can obtain the local incident angle β_w, the angle of attack α_b, and the speed of the wind V_r on the blade element on the right wing as follows

$$\beta_w(r,t) = \tan^{-1}\frac{-V_{wz}}{V_{wx}} \tag{35}$$

$$\alpha_w(r,t) = \theta_w(t) - \beta_w(r,t) \tag{36}$$

$$V_r^2(r,t) = \sqrt{V_{wx}^2 + V_{wz}^2} \tag{37}$$

where we neglected the flow along the wing span V_{wy} and the wing rotation $\theta_w(t)$ controller can be properly designed to yield a positive angle of attack for both upstroke and downstroke motions (see Fig. 5b).

The x and z directional forces F_{wx} and F_{wz} on the wing frame given in (26), computed with dL, dD in(24) and dL_{rot} in (25), can be transformed into the forces in the vehicle body frame:

$$\mathbf{F}_{\text{right}} = \begin{pmatrix} F_x \\ F_y \\ F_z \end{pmatrix}_{\text{right}} = \mathbf{T}_{bs}(\Theta_s)\mathbf{T}_{sw}(\phi_w, \psi_w) \begin{pmatrix} F_{wx} \\ 0 \\ F_{wz} \end{pmatrix}_{\text{right}} \tag{38}$$

where we added the subscript *right* to indicate that this force vector is from the right wing. A similar expression can be obtained for the left wing ($\mathbf{F}_{\text{left}}$). Note that each wing has different wing angular parameters such as ϕ_w, ψ_w, and θ_w, although the stroke plane angle Θ_s is the same for both wings. In symmetric wing motions, the F_y forces from both wings cancel each other.

In order to compute the rotational moments generated by the aerodynamic forces, we first calculate the position of the wing blade element with respect to the body frame

$$\mathbf{p}(r) = \mathbf{T}_{bs}(\Theta_s)\mathbf{T}_{sw}(\phi_w, \psi_w) \begin{pmatrix} 0 \\ r \\ 0 \end{pmatrix} + \begin{pmatrix} d_x \\ d_y \\ d_z \end{pmatrix} \tag{39}$$

where d_x and d_z indicate the origin of the stroke plane frame in the body frame.

Then, we can compute the aerodynamic moments with respect to the c.g.

$$\begin{pmatrix} dM_x \\ dM_y \\ dM_z \end{pmatrix} = \mathbf{p}(r) \times \left(\mathbf{T}_{bs}(\Theta_s)\mathbf{T}_{sw}(\phi_w, \psi_w) \begin{pmatrix} -(dL + dL_{rot})\sin\beta_w - dD\cos\beta_w \\ 0 \\ dD\sin\beta_w - (dL + dL_{rot})\cos\beta_w \end{pmatrix} \right) + \begin{pmatrix} dM_{x0} \\ dM_{y0} \\ dM_{z0} \end{pmatrix} \tag{40}$$

$$\begin{pmatrix} dM_{x0} \\ dM_{y0} \\ dM_{z0} \end{pmatrix} = \mathbf{T}_{bs}(\Theta_s)\mathbf{T}_{sw}(\phi_w, \psi_w)\mathbf{T}_{\theta_w}(\theta_w)\frac{1}{2}\rho V_r^2 c(r)dr \begin{pmatrix} rc_{l0} \\ c(r)(c_{m0} + c_{\alpha,w}\alpha_w) \\ rc_{n0} \end{pmatrix} \tag{41}$$

$$M_x = \int_{r=0}^{R} dM_x, \quad M_y = \int_{r=0}^{R} dM_y, \quad M_z = \int_{r=0}^{R} dM_z \tag{42}$$

where dM_{x0}, dM_{x0}, and dM_{x0} denote the constant aerodynamic moments that include the moment at the mean aerodynamic center, computed by the moment coefficients c_{l0}, c_{m0}, $c_{\alpha,w}$, and c_{n0}. Also, R is the wing span. The additional transformation $\mathbf{T}_{\theta_w}(\theta_w)$ rotates the wing frame about the y_w axis by the wing pitch rotation angle θ_w.

III.C. Dynamic Modeling

By combining all the forces and moments from the right wing and the left wing, we can derive 6-DOF equations of motion for the flapping flying MAV in the body frame, whose orientation with respect to the inertial frame is described by the Euler angles. We assume the moment of inertia of the wing compared to the body weight is negligible. Then, we can obtain the following set of equations. The translational motion of the c.g. of the flapping flying vehicle driven by the aerodynamic force terms in (38) can be expressed as

$$m\dot{\mathbf{V}}_b + m\boldsymbol{\Omega}_b \times \dot{\mathbf{V}}_b = \mathbf{T}_{be}(\phi_b, \theta_b, \psi_b)\mathbf{F}_g + \mathbf{F}_{\text{right}} + \mathbf{F}_{\text{left}} + \mathbf{A} \tag{43}$$

where $\mathbf{V}_b = (V_{bx}, V_{by}, V_{bz})^T$ denotes the vehicle velocity vector in the body frame, $\boldsymbol{\Omega}_b = (p, q, r)^T$ is the body angular rate, and the Euler angular transformation matrix determines the orientation of the body frame with respect to the inertial frame

$$\mathbf{T}_{be}(\phi_b, \theta_b, \psi_b) = \begin{bmatrix} \cos\theta_b\cos\psi_b & \cos\theta_b\sin\psi_b & -\sin\theta_b \\ \sin\phi_b\sin\theta_b\cos\psi_b - \cos\phi_b\sin\psi_b & \sin\phi_b\sin\theta_b\sin\psi_b + \cos\phi_b\cos\psi_b & \sin\phi_b\cos\theta_b \\ \cos\phi_b\sin\theta_b\cos\psi_b + \sin\phi_b\sin\psi_b & \cos\phi_b\sin\theta_b\sin\psi_b - \sin\phi_b\cos\psi_b & \cos\phi_b\cos\theta_b \end{bmatrix}.$$

In addition, $\mathbf{F}_g = (0, 0, mg)^T$ is the gravitational force vector in the inertial frame, while $\mathbf{F}_{\text{left}}$ and $\mathbf{F}_{\text{right}}$ denote the aerodynamic forces from each wing, obtained from (38). Note that each wing has different wing angular parameters such as ϕ_w, ψ_w, and θ_w, although the stroke plane angle Θ_s is the same for each wing. The force vector $\mathbf{A} = (A_x, A_y, A_z)^T$ represents the additional forces generated by the body (fuselage) and the tail.

The equations of rotational motion are driven by the aerodynamic moments $\mathbf{M}_{\text{right}}$ and $\mathbf{M}_{\text{left}}$ of each wing that can be obtained from (40)

$$\mathbf{I}_b\boldsymbol{\Omega}_b + \boldsymbol{\Omega}_b \times (\mathbf{I}_b\boldsymbol{\Omega}_b) = \mathbf{M}_{\text{right}} + \mathbf{M}_{\text{left}} + \mathbf{B} \tag{44}$$

where $\mathbf{I}_b$ is a 3×3 inertia matrix and the additional torque vector $\mathbf{B} = (B_x, B_y, B_z)^T$ represents the aerodynamic moment from the body and the tail. The relationship between the body angular rate $\boldsymbol{\Omega}_b =$

$(p, q, r)^T$ and the Euler angle vector $\mathbf{q}_b = (\phi_b, \theta_b, \psi_b)^T$ can be determined by

$$\begin{pmatrix} \dot{\phi}_b \\ \dot{\theta}_b \\ \dot{\psi}_b \end{pmatrix} = \mathbf{Z}(\mathbf{q}_b)\mathbf{\Omega}_b = \begin{bmatrix} 1 & \sin\phi_b \tan\theta_b & \cos\phi_b \tan\theta_b \\ 0 & \cos\phi_b & -\sin\phi_b \\ 0 & \sin\phi_b \sec\theta_b & \cos\phi_b \sec\theta_b \end{bmatrix} \begin{pmatrix} p \\ q \\ r \end{pmatrix} \tag{45}$$

Note that any other orientation representations such as quaternions can be used in lieu of the Euler angles in the preceding equations. Also, any disturbance force and torque can be added to the equations.

IV. CPG-based Flapping Flight Control and Simulation Results

The aim of this section is to show that CPG-based flight control can stabilize and control flapping flight dynamics given in Section III.C by using the synchronized and symmetry-breaking (phase difference) oscillatory motions of two main wings. In particular, we show that the dynamics can be effectively controlled without using aerodynamic control surfaces such as ailerons, elevators, rudders, and directional control of tail wings.

The example presented in this paper is alternating two different flight modes of flapping and gliding flight. We maintain a particular interval of altitude level, bracketing steady level flight. Longitudinal and lateral motions are nearly uncoupled, so we consider only longitudinal motion for brevity. Lateral forces are therefore considered symmetric. Additionally, we do not consider the aerodynamics of the second joint and instead assume each wing to be one rigid piece. That is, in (33), we set

$$\Big(x_w(r), \quad y_w(r), \quad z_w(r)\Big)^T = 0. \tag{46}$$

This restricted kinematic and dynamic model is constructed in Simulink, allowing us to demonstrate how simple longitudinal stability can be obtained for flapping flight driven by a CPG network. From biological investigation, Thomas and Taylor[66] suggest that many birds utilize the ability to twist their wings in order to provide a wash-out and backward-sweep combination or a wash-in and forward-sweep combination for gliding stability. This configuration can provide inherent tailless longitudinal stability. Alternatively, they suggest that birds dynamically alter the wing sweep in order to obtain longitudinal stability in gliding flight. Our experimental apparatus is untwisted, so we choose the second method for stability in our simulations.

Gliding Mode: We assume that in gliding flight there is no reciprocal flapping motion, obviously. Therefore, we set the parameter $\omega(t)$ in the Hopf oscillator to zero. In addition, we set the coupling gains between CPGs to zero. This provides us simple control of our wing by exploiting the bifurcation in Hopf oscillators, causing them to snap to a single value corresponding to the bias. We further assume that we are able to select an optimum wing angle of attack with regard to the wing size and aerodynamics, vehicle weight and velocity to maximize the glide path angle. We can then control the lead lag motion (ψ_w) and flapping angle (ϕ_w) by their bias parameters. With zero $\omega(t)$, these parameters should tend to their bias values in a non-oscillatory manner. A negative (positive) flapping angle or negative (positive) lead-lag angle can provide a pitch-down (pitch-up) moment due to drag or lift, respectively. We have therefore reduced control dimensionality to three actively controlled parameters: wing pitch, wing flapping angle, and lead-lag angle. In fact, depending on the physical characteristics of the specific vehicle, controlling only one of wing flapping angle or lead-lag angle could be sufficient for gliding stability.

Flapping Flight Control by Flapping Frequency: Seemingly more difficult than stability in gliding flight is stability in flapping flight. We propose a novel control law unique to our CPG set-up which reduces control dimensionality to only two parameters. The first parameter is the oscillation frequency $\omega(t)$ of the coupled Hopf oscillators in (6). By inspecting the definitions of the local angle of attack of the wing blade element α_w given in (20) and (35), we can find that $\omega(t)$ correlates with flapping frequency, which in turn correlates with increased lift and thrust. Those in turn, correlate with forward (V_{bx}) and vertical (V_{bz}) velocity of the body, all other factors being equal. We can very simply control ω with the old adage, "If you want to go faster, press the pedal further." For example, we can consider the following control law

$$\omega = K \int_0^t \dot{\omega} dt = K \int_0^t \left(V_{x,desired} - V_{x,actual}\right) dt \tag{47}$$

We can use the following corollary to show that the time-varying $\omega(t)$ does not alter the synchronization proof of the oscillators.

Corollary 1 *From the dynamic equation of the Hopf oscillator in (1), the time-varying $\omega(t)$ does not affect the stability proof for Theorem 2*

Proof 3 *Since the symmetric part of $\mathbf{f}$ cancels the ω term and ω does not change the maximum eigenvalue of $\mathbf{V}^T[\mathbf{f}]\mathbf{V}$. The rest of the proof follows Theorem 2.*

Control of ω takes care of translational forces, but we have not yet considered rotational moments. It should be noted that the control of the maximum flapping stroke angle $\phi_{w_{max}}$, e.g., $\rho_1 = \rho_5$ for the CPG configuration in Fig. 4a, can be also used to induce similar translational control effects.

Flapping Flight Control by Phase Differences: Our second control parameter is the phase difference between the lead-lag CPG and the pitching CPG $\Delta_{31} - \Delta_{21}$ in Figure 4a. or simply Δ_{32}. Note that when we do take the second joint into account for the dynamic modeling, we can add an additional performance parameter for the phase difference between lead-lag angle (ψ_w) and the second joints (ϕ_{w2}), with an accompanying change in the phase difference between the first and second joints to retain flow invariance. Effectively, all phase differences can be altered as long as flow invariance is retained. Different graph configurations may be required to obtain favorable characteristics for high-agility maneuvers and Theorem 2 can be used to derive the exponentially and globally stabilizing gains. Additionally, our oscillator stability proof in Theorem 2 assumes constant or relatively slowly varying phase differences. However, the error terms from the additional time-varying parameters other than $\omega(t)$ can be obtained by the robust contraction analysis,[60] which shows the boundedness of the synchronization error.

Corollary 2 *For time-varying phase differences Δ_{ij}, the synchronization of the rotated Hopf states $\{\mathbf{z}\}$ globally converges to the bounded error defined by $\mathbf{V}^T\mathbf{T}\dot{\mathbf{T}}^{-1}\{\mathbf{z}\}$.*

Proof 4 *Recall the relationship between the original Hopf variables $\{\mathbf{x}\}$ and $\{\mathbf{z}\} = \mathbf{T}(\Delta_{ij}, \rho_i)\{\mathbf{x}\}$ in (10). Since the function $\dot{\mathbf{T}}(\Delta_{ij}, \rho_i)$ is nonzero, (14) becomes*

$$\{\dot{\mathbf{z}}\} + \mathbf{T}\dot{\mathbf{T}}^{-1}\{\mathbf{z}\} = \mathbf{T}\left[\mathbf{f}(\{\mathbf{x}\}; \rho)\right] - k\mathbf{L}\{\mathbf{z}\} \tag{48}$$

Consequently, the virtual system in (18) becomes

$$\dot{\mathbf{y}} = \mathbf{V}^T\left[\mathbf{f}(\mathbf{V}\mathbf{y} + \mathbf{1}\mathbf{1}^T/n\{\mathbf{z}\}; \rho_1)\right] - k\mathbf{V}^T\mathbf{L}\mathbf{V}\mathbf{y} + \epsilon(t) \tag{49}$$

where the error term $\epsilon(t)$ comes from the nonzero time-derivative of the $\boldsymbol{T}$ matrix since some Δ_{ij} is time-varying.

$$\epsilon(t) = -\mathbf{V}^T\mathbf{T}\dot{\mathbf{T}}^{-1}\{\mathbf{z}\} \tag{50}$$

Hence, although the $\mathbf{y}$ system in (49) is contracting, the Hopf oscillators do not perfectly synchronize because $\mathbf{y} = 0$ is no longer the particular solution. By robust contraction analysis,[60] where $P_1(t)$ defines represents a desired system trajectory and $P_2(t)$the actual system trajectory in a disturbed flow field given in (18 with the error term. Also, consider the distance $R(t)$ between two trajectories $P_1(t)$ and $P_1(t)$ such that

$$\dot{R}(t) + \ell R(t) \leq \|\epsilon(t)\| \tag{51}$$

where $\ell > 0$ is the contraction rate of the virtual system (49) such that $\ell = k\lambda_{min}(\mathbf{V}^T(\mathbf{L} + \mathbf{L}^T)/2\mathbf{V})) - \lambda$. Hence, the synchronization error converges to the ball of the radius $\|\epsilon(t)\|$ /ℓ

To simply characterize the effectiveness of altering the phase difference between flapping and lead-lag, consider the largest force values over the length of a stroke. These are likely to be obtained from lift in the middle of a downstroke. With a zero bias lead-lag and a center of gravity coinciding with the stroke plane, a phase difference of 270° between the flapping CPG and the lead-lag CPG gives Azuma's[3] elliptical model of flapping: negative lead-lag on downstroke, positive lead-lag on upstroke. The simplest analysis combines a maximum force with the most-negative lead-lag at the middle of the downstroke to predict a large pitch-down moment on the body. Alternatively, if we set the phase difference to 180°, we see the maximum force coinciding with the maximum positive lead-lag at the middle of the downstroke, predicting a large pitch-up

moment. We use this as our primary control variable for longitudinal stability. For the following figures, we fix $\Delta_{21} = 90°$. We tune our range to

$$\theta_{body}\colon\ [-2°, 2°] \rightarrow \Delta_{31}\colon\ [180°, 270°] \tag{52}$$

by

$$\Delta_{31} - \Delta_{21} = -45°\theta_{body} + 135° - K\dot{\theta}_{body}. \tag{53}$$

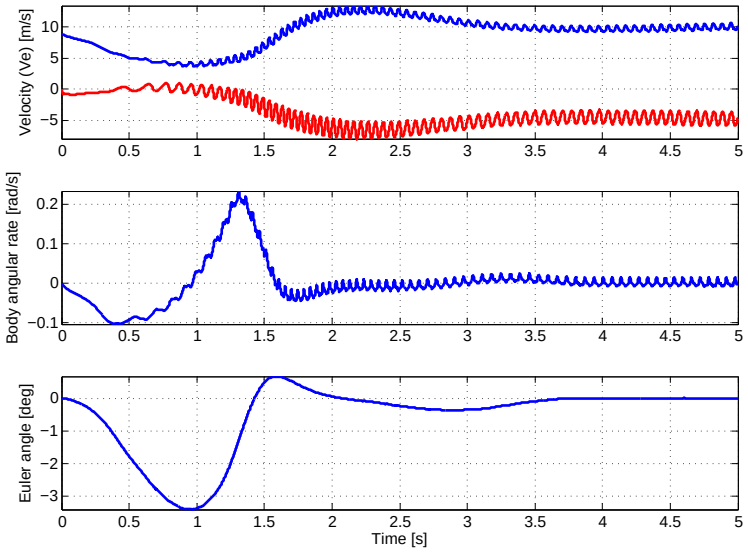

Figure 7. State vectors of the two alternating flight modes, flapping and gliding.

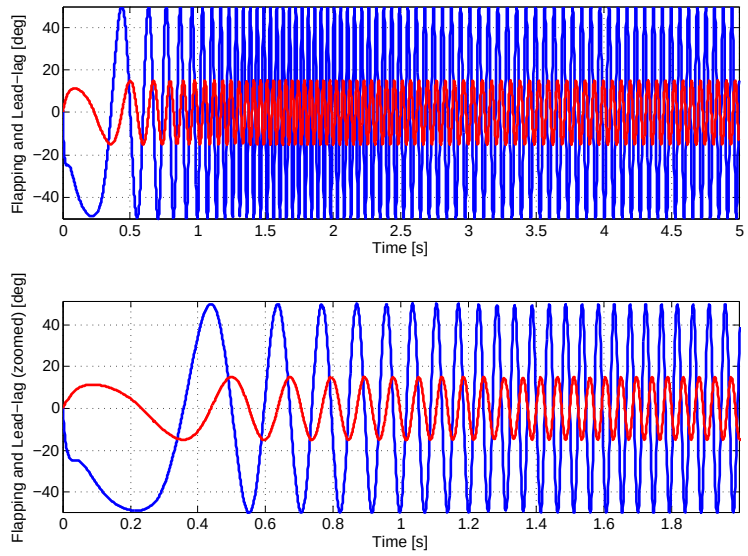

Figure 8. Flapping (ϕ_w) and lead-lag angles (ψ_w) of the two alternating flight modes, flapping and gliding.

The body states resulting from these control laws are seen in Figure 7 and the control parameters are in Figure 10. Note that we have put saturation limits on the phase difference at our limiting values of $\pi/2$ and π. Figure 8 shows the resulting oscillatory behavior of the flapping and lead-lag motion and highlights the effects of our changing control variables on CPG behavior. The longitudinal motion is stabilized, confirming the suspicion of Thomas and Taylor[67] that birds may act more like tailless aircraft than conventional tailed

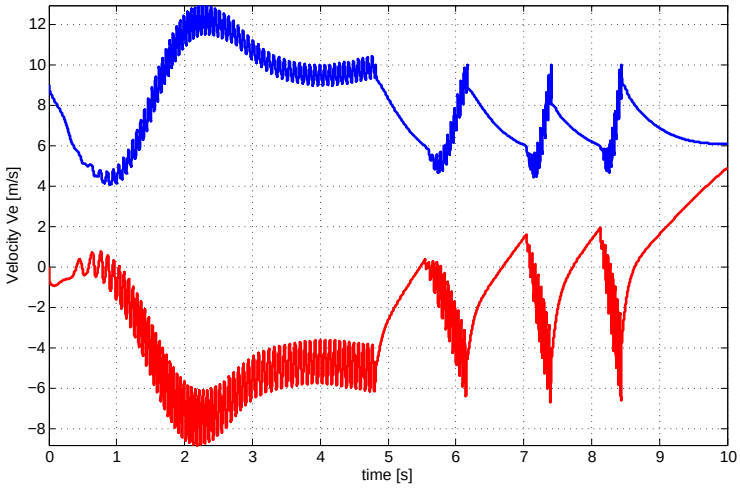

Figure 9. Velocity vector of the two alternating flight modes, flapping and gliding.

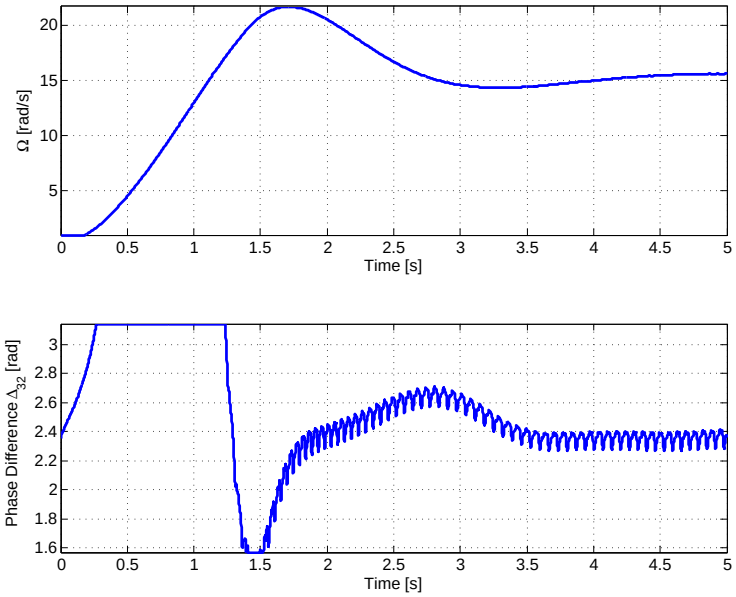

Figure 10. Control inputs of the two alternating flight modes, flapping and gliding.

aircraft. This model has no stabilizing tail-induced moment and therefore sheds light on the fact that many birds can fly without their tail. Including a constant or angle of attack dependent body/tail moment will only serve to alter the equilibrium point. Altering the range through which we control the phase difference allows us to tune the equilibrium point as we desire for any body/tail behavior.

Returning to altitude stabilization, we propose switching between flapping mode and gliding mode. Our requirements for switching use the current Ω to determine what mode we are in, as well as altitude and velocity information to determine whether to switch mode. Recalling that the z-direction is positive downward, we set the test for gliding mode as

$$\begin{aligned} \text{if } (\omega > 0 \ \ \& \ \ Y_b < -20 \ \ \& \ \ V_{bx} > 10) \text{ or } (\omega = 0 \ \ \& \ \ Y_b < -10 \ \ \& \ \ V_{bx} > 6) \\ \text{then glide } (\omega = 0) \\ \text{else flap } (\omega \neq 0). \end{aligned} \tag{54}$$

This switching ensures that we have sufficient altitude and forward velocity to glide, but will interrupt the constant ascending flapping flight in figure 7 with periods of gliding. The result is shown in figure 9, and it is apparent that the vertical velocity now switches between positive and negative to provide altitude control.

In the future, as our flight requirements demand more agile maneuvers than simple ascending, constant forward velocity flight, we will also investigate the use of lead-lag bias and flapping angle bias to provide even larger moments for more rapid longitudinal response. Lead-lag bias will operate similarly to gliding flight, as the mean lift force is positive. Flapping bias will operate opposite of gliding, as the mean horizontal force is a thrust, rather than a drag. It should be noted that with the CPG model, we have plenty of control dimensionality available, yet active control is shown to only be needed on a few parameters to provide stability. This is in keeping with the goals of CPGs to reduce bandwidth required by outer-loop navigation control. In particular, we have control over ρ and a for each Hopf oscillator, $\omega(t)$, the stroke plane Θ_s, as well as the connectivity structure and phase differences. Given four Hopf oscillators and the graph structure of Figure 4a, we have a total of 17 potential control parameters. While many of these can remain constant, much optimization can occur, particularly with respect to controlling wing pitch for optimal lift and thrust characteristics.

V. Robotic Bat: Novel Flapping Mechanism for Experimental Validation

We show the functionality of the 10-DOF robotic bat with 12 control variables to act as a testbed for the experimentation of multiple types of control and aerodynamic studies in flapping flight. Experiments are performed using a partially complete 8-DOF model which has full control over wing pitch, lead-lag and flapping frequency as well as the independent flapping amplitude for each wing (see Figures 11 and 12). To quantitatively validate the control schemes being tested, we test the model in the 8×6-ft wind tunnel at Iowa State University. Aerodynamic forces and moments will be measured by a three-axis force-torque sensor. A real time dSPACE controller is used to gather data as well as run the CPG-based control law. Using the extensive wind tunnel facilities, which has a high-resolution particle image velocimetry (PIV) system and stereo high-speed cameras, and the complex robotic bat model developed, we outline how further experimentation is possible to test the effects of morphological flight parameters, complex wing shapes, and compliant wing technologies.

V.A. Biological Inspiration

Flight has historically been inspired from nature; birds in flight formed the basis of all early attempts at flight. Therefore there are several important examples of flight in nature which we derive our flapping design from. Insects have been a popular choice because of the relatively simple configuration of their flight system. They require only two control inputs (stroke angle and pitch angle) which can be modeled as a simple sinusoid. Unfortunately, the aerodynamics of insect flight vary significantly from the mechanics of bat flight and bird flight. Unsteady effects dominate their flight regime because of the extremely low Reynolds number. Insect wings are typically very simple in shape and mostly rigid. Even though an insect wing may be considered rigid in the biological world, even these wings are more compliant than their fixed wing aircraft counterparts. Insects also have very few muscles to control the trajectory of their wing, and they are all located in the shoulder.

(a) (b) (c)

Figure 11. A 10-DOF robotic bat that has 12 control variables and sophisticated flapping wings. If we install membrane wings, the hind-leg joints control the tension of the membrane wings.

Bird flight is more complex because the wing becomes more complex. The addition of light weight bone structures into the wing, the complex airfoils formed by the feathers, and the addition of the elbow and wrist joints make birds much more difficult to simulate. Their flight mechanics also differ significantly from insects as well. Bird flight spans a large range of mechanisms. Humming birds are small and heavily rely on unsteady effects to maintain their amazing but energetically costly hovering performance. Larger birds which are specialized for traveling long distances rely much more on soaring and the use of air currents, with flapping propulsion being used sparingly to conserve energy. In between these extremes lie many other types of birds, some specialized for agility and others specialized for diving or high speed. Birds have muscles located mostly inside their body acting on the shoulder joint. There are smaller muscles inside the arm allow the actuation of the elbow and wrist joints to control the wings shape during the flapping stroke. The range of motion of the joints on the wing is limited, but adequately modeled by the degrees of the freedom described in Figures 2 and 4.

Bats present an interesting differentiation from both birds and insects. They operate in a Reynolds number range where unsteady effects are important at low speeds but decreasingly important at the higher range of flight speeds. They have highly compliant wings that flex differently in the chordwise and spanwise directions.[68] The tension on the wing membrane is controlled by a combination of several joints, the legs and the numerous finger joints. Larger species of bats behave similarly to large birds, relying more on soaring than flapping. Smaller bats, specialized as insect hunters, have developed extremely high agility and flap continuously. Because bats are equally or even more complicated than birds, and because of their incredible flight performance, we have chosen to model our robotic testbed after a bat. Bat flight is also well suited to CPG-based flapping flight control because it relies heavily on the synchronization of phase between several different oscillatory motions.

V.B. Mechanical Design

The flapping flight testbed was designed as a highly controllable, non-flying test platform modeled after the kinematics of a bat. The mechanism provides a total of ten degrees of freedom and twelve control degrees of freedom, three angles in each shoulder joint, one in each leg, and one flapping amplitude control servo and flapping DC motor in each wing. Shoulder joints are also analogous to our own shoulder joints, able to move forward, backwards (lead-lag), up, down (flapping), and can twist in both directions (pitch). The hind-legs move in a similar fashion without the ability to twist. These 10 degrees of freedom are combined with variable speed flapping motors to allow for maximum flexibility in control schemes. The main up-down reciprocating flapping motion of the wings are independently powered by two 8 watt Maxon motors with 19:1 gear ratios. This ratio allows us to use the entire range of the motors and gives us the torque required to move large wings. Electronic motor controllers for the two Maxon motors allow for precise control of motor velocity and therefore wing flapping frequency. All other degrees of freedom are directly controlled with Hitec feather servos.

The flapping amplitude is varied by a moving crank arm and a rotating slider mechanism, unique to our design (see Fig. 12). This mechanism is repurposed from a commercial part used on RC helicopter tail rotors. As the slide moves it varies the distance from the motor shaft to the crank arm and changes the amplitude of the flapping. The crank arm is actuated by a feather servo. This servo does not have to move within the flapping stroke to maintain the flapping amplitude unless a non-sinusoidal waveform is desired.

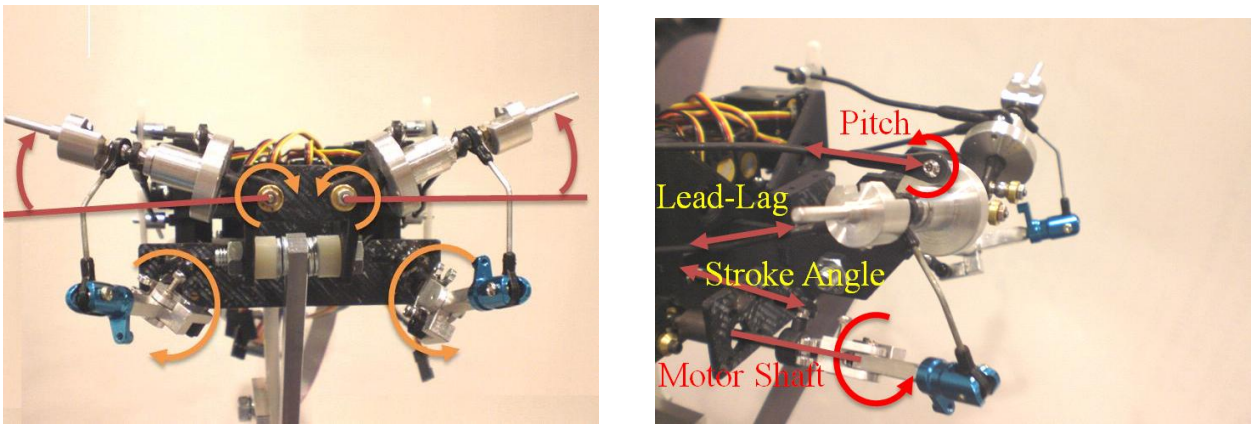

(a) (b)

Figure 12. A 10-DOF robotic bat (with 12 control variables) MAV with independent flapping frequency and max amplitude control for each wing along with pitch and lead-lag angle servos. The hind-lag servos are not shown.

Additionally, the servo has to move only a small angular distance which greatly decreases the requirements for servo speed if the flapping frequency is high. The lead-lag and pitch servos have to move significant distances but because the flapping motion is powered by the DC motor the load applied to these servos is significantly less. This allows us to use considerably cheaper RC servos rather than expensive robotics servos.

The main frame of the testbed was initially created using rapid prototyping methods. This method allows for quick changes in the design to be made, along with complex parts that rival those allowed for by machining. Because of extensive coupling between the different degrees of freedom it is desirable to be able to adjust the dimensions of the frame to attain the target ranges of motion. The new platfrom using a final frame, requiring precise dimensioning and specific materials, can be created using CNC machining methods. All drive train materials are aluminum or steel, with non standard drive train parts being machined. Care was taken in the design to provide multiple mounting positions for servos and hind legs to facilitate the easy change of parameters.

The legs are actuated by two feather servos allowing for two degrees of freedom. The legs are attached to the bottom portion of the wing and allow us to emulate the bats ability to vary tension across it's wing membrane. Because bats use a compliant wing, it is important to be able to vary the tension which indirectly varies how much the wing stretches.[68] Little has been done to research the effect of the legs specifically on a bats compliant wing so two degrees of freedom have been left to allow experimentation. If an optimal plane of motion can be found the legs can be reduced to a single degree of freedom to save weight.

V.C. Experimental Setup

The experimental setup used consists of three major functional units: the dSPACE controller and PC, the robotic bat model and the wind tunnel facility. They are described in Fig. 13.

In order to conduct real time hardware in the loop simulations using the CPG controller it was necessary to use a real time controller. We are using a dSPACE RT1104 to measure the outputs of the 6DOF force-torque sensor and generate the motor outputs. Our RC servos require a PWM signal to control their position which was generated from the dSPACE PWM generators. The flapping motor controllers are configured to allow step inputs. In this mode the motors behave as position controlled servos with the rising edge of a square pulse moving the servo a single encoder step. If a pulse train is formed then the frequency of the pulses will command a fixed frequency. In order to vary the flapping frequency we use a square wave generator on the dSPACE to generate waves of different frequencies.

The dSPACE real time controller also allows us to program the CPG controller in Simulink and compile it to run on the controller. The control system is executed at fixed time steps which are programmable. The controller also contains the analog to digital converters which measure the force-torque sensor outputs. The dSPACE consists of two units, the processor unit inside the desktop PC and the signal conditioning unit which has the connectors and necessary signal protection circuitry. Because the processor unit runs inside the PC we can log all the outputs directly to the computer for post processing in MATLAB.

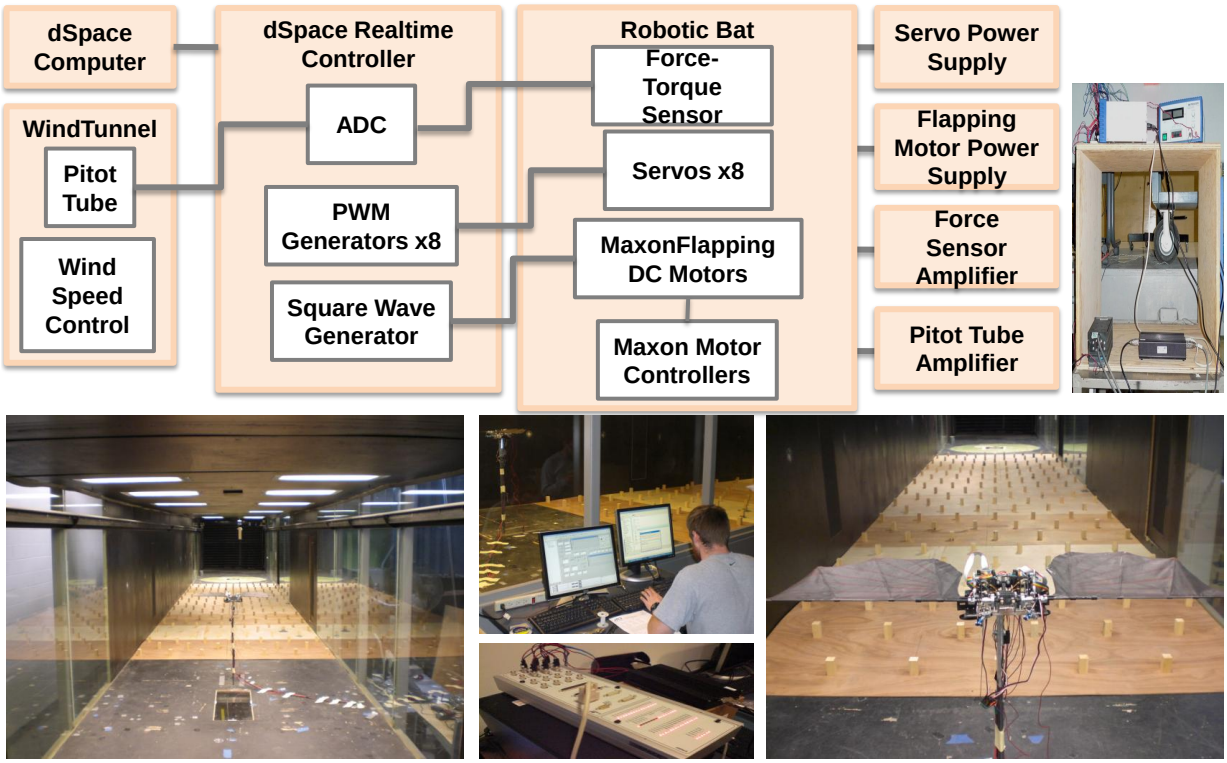

Figure 13. Schematic of the experimental set-up using the robotic bat in the wind tunnel.

The robotic bat is described in mechanical detail in previous sections. For testing in the wind tunnel it was necessary to extend cabling to run outside the tunnel. The cables run along a test stand fabricated specifically for wind tunnel usage. The main shaft extending from the floor to the bat is a steel tube pressed to the shape of an airfoil. This keeps the effects of the test stand to a minimum which most importantly minimizes vibrational effects on the bat which are exaggerated by the nature of flapping flight itself. The mount also allows us to vary the body angle of attack along with free stream velocity for characterizing aerodynamic properties.

The Aerodynamic/Atmospheric Boundary Layer (AABL) Wind and Gust Tunnel at Iowa State University is part of the extensive wind tunnel complex available in Wind Simulation and Testing (WiST) Laboratory. The wind tunnel has a test section 8 ft wide and 6 ft high and is capable of speeds up to 47 m/s. Tests were conducted up to 8 m/s. The free stream velocity was measured with a pitot tube to ensure the accuracy of measurements.

V.D. Preliminary Wind Tunnel Test Data Acquisition and Analysis

The CPG network described in Figure 4a is constructed as a Simulink model and incorporated in the dSPACE realtime controller along with other hardware described in the previous section. We present a preliminary result that validates the synchronized motion of the CPG-based control of the robotic bat flapping wing testbed. Further tests that measure more accurate aerodynamic coefficients are underway. For the tests described here, we did not connect the hind legs since the membrane wings have yet to be installed.

Figures 14 and 15 show results of the experimentation of the robotic bat whose half wing span is 34 cm (see Fig. 13). The robotic bat is mounted horizontally. The first rows show the horizontal and vertical forces measures from the force-torque sensor, the second row shows the pitch (θ_w) oscillation, the third row is the wind speed of the wind tunnel, and the fourth row is the common oscillation frequency (in rad) of the coupled Hopf oscillator. In Figure 14, the pitch motion was activated in 30 sec. and the combined pitch (θ_w) and flapping (ϕ_w) increase the lift (F_z) by more than a factor of two. This shows that the pitch control is indispensable and more experiments are underway to find the most efficient phase difference (Δ_{21}), which

can be compared with Dickinson's experimentation with robotfly (advanced rotation with $\Delta_{21} = 90+\delta$ deg). Figure 15 shows the variation of the aerodynamic forces when the oscillation frequency ω and the forward velocity V_∞ are varying. As predicted in Sections III and IV, the ω is correlated with the forward speed but they were independently varied in this wind tunnel test. As the flapping frequency ω jumped from 1.7Hz to 2.9Hz at 80 sec., the lift force F_z increases from 0.65N to 1N, while the variation of the wind speed from 3.1 m/s to 4.2 did not change the aerodynamic forces dramatically. While the DC motors smoothly varies the main flapping oscillation ϕ_w, the use of the CPG network was able to generate smooth variations of the pitch oscillation. This is critical especially since we were using the RC servo motors for the pitch rotations of both wings.

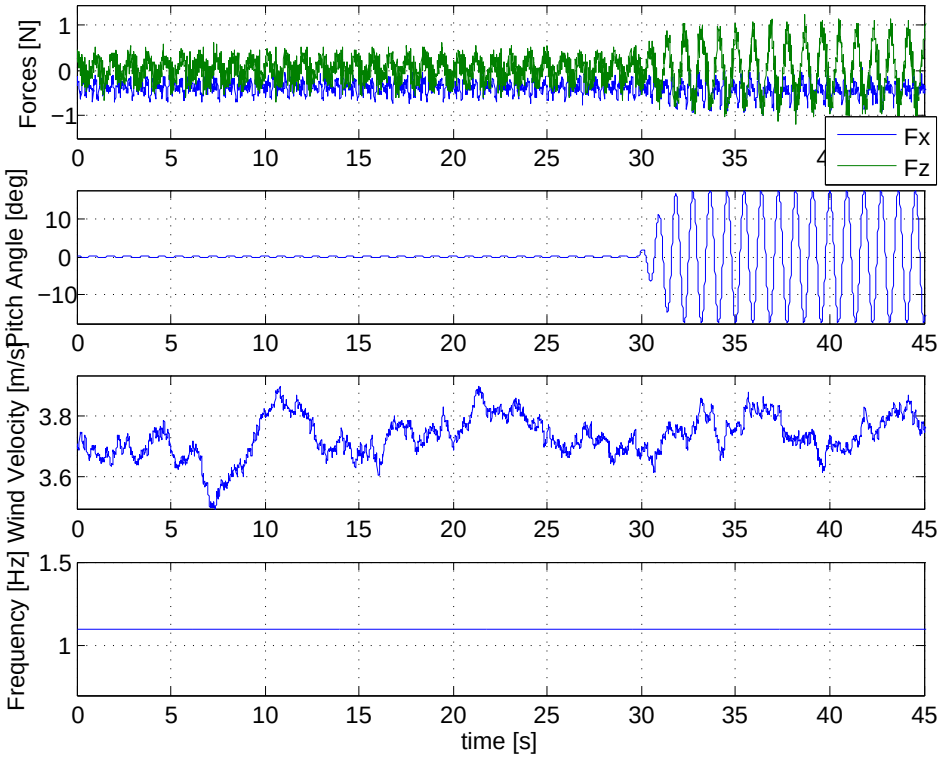

Figure 14. Impact of the synchronized pitch θ_w oscillation.

VI. Conclusion

We investigated the hypothesis that the adaptive control and synchronization of coupled nonlinear oscillators, inspired by central pattern generators (CPGs) found in animal spinal cords, can effectively produce and control stable flapping flight patterns and can be used to stabilize the vehicle dynamics. We also presented numerical simulation and experimentation by using a realistic vehicle model. An engineered CPG network, which ensures the stability and robust adaptation of motion, can significantly reduce the complexity associated with flapping flight.

Central to the agile flight of natural flyers is the ability to execute complex synchronized three-dimensional motions of the wings as shown in Figure 2. In this paper, we introduced a mathematical and control-theoretic framework of CPG control theory that enables such synchronized wing maneuvers. Because of the oscillatory nature of flapping flight it is very important to have a control law which allows for very smooth changes in flapping frequency. We show that CPGs can generate the necessary wing trajectories and actuator waveforms to control a flapping flight MAV. Additionally they allow for stable but rapid changes in flapping parameters such as wing pitch and the lead-lag angle.

In order to validate this control scheme it was necessary to build a capable flapping flight testbed. While currently this testbed is not capable of flying, it allows wind tunnel testing to commence. Using the real time

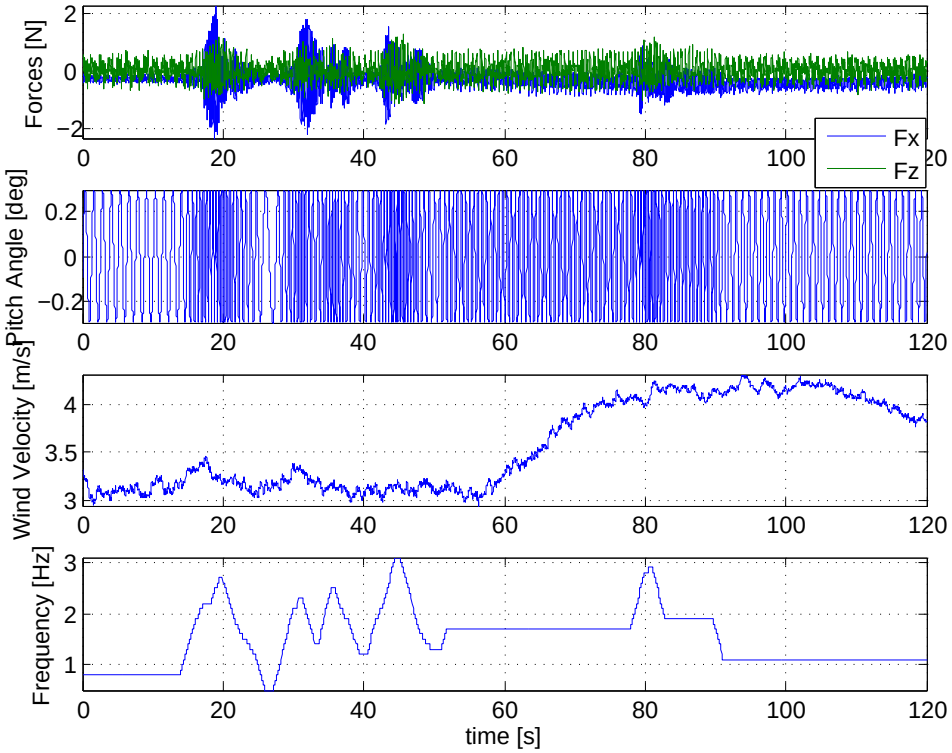

(a) 0 to 120 sec

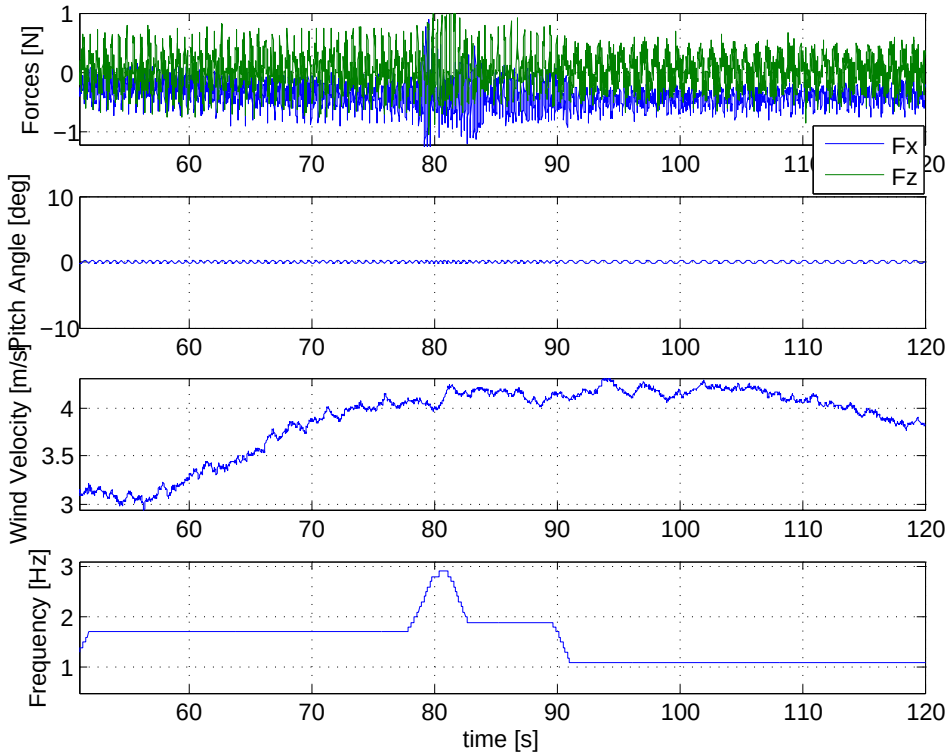

(b) 50 to 120 sec

Figure 15. Impact of the oscillation frequency ω and wind speed.

controller we were able to conduct hardware-in-the-loop simulations using the CPG control laws. From the data collected by this testing we are able to show that CPGs do allow for the smooth transitions of control parameters, as well as generating useful wing trajectories.

The dynamic model and wing kinematic model of flapping flight were developed which represents the more complete and complex mechanical flapping system developed for wind tunnel testing. This dynamic model includes a tilted stroke angle, the lead-lag motion, and the relative body velocity, in addition to the stroke and pitch angles. The complete model includes all the degrees of freedom possessed by the robotic bat model.

Finally, the robotic bat model that has been developed provides a useful contribution to the state of the art. Previous models have been very limited by mechanical simplicity to generating only sinusoidal waveforms. Our model allows not only allows experiments involving motions not used before such as lead lag, but also for experiments with non-sinusoidal waveforms. This bat model allows for additional research involving compliant wings and other biologically inspired research. Coupled with the power of CPG control this allows for exploration of more sophisticated nonlinear flight control.

Acknowledgements

This project was supported by the Air Force Office of Scientific Research (AFOSR) under the Young Investigator Award Program (YIP) (contract monitor: Dr. Willard Larkin). This paper benefitted from discussion with Profs. Jean-Jacques Slotine at MIT, Prof. Kenneth Breuer at Brown University, and Dr. Gregg Abate at the Air Force Research Lab. The first author appreciate Prof. Partha Sarka at Iowa State University for allowing him to use the wind tunnel facility in the Wind Simulation and Testing Laboratory. The authors gratefully acknowlege contributions from the following students at Iowa State University: Anid Monsur, Antonella Albuja, Brad Smith, Christopher Massina, Keegan Gartner, Matt Hawkins, Merritt Tennison, and Ryan Paul.

References

[1]T. J. Mueller, e. a., *Fixed and Flapping Wing Aerodynamics for Micro Air Vehicle Application*, 2001, *Progress in Astronautics and Aeronautics*, AIAA.

[2]Shyy, W., Lian, Y., Tang, J., Viieru, D., and Liu, H., *Aerodynamics of Low Reynolds Number Flyers*, Cambridge University Press, New York, NY., 2008.

[3]Azuma, A., *The Biokinetics of Flying and Swimming*, AIAA, 2nd ed., 2006.

[4]Kato, N. and Kamimura, S., *Bio-Mechanisms of Swimming And Flying: Fluid Dynamics, Biomimetic Robots, And Sports Science*, Springer Verlag, 2008.

[5]Norberg, U. M., *Vertebrate Flght: Mechanics, Physiology, Morphology, Ecology and Evolution*, Springer-Verlag, 1989.

[6]Dickinson, M. H., Lehmann, F. O., and Sane, S. P., "Wing Rotation and the Aerodynamic Basis of Insect Flight," *Science*, Vol. 284, 1999, pp. 1954–1960, June .

[7]Swartz, S. M., "Allometric Patterning in the Limb Skeleton of Bats: Implications for the Mechanics and Energetics of Powered Flight," *J. Morph.*, Vol. 234, 1997, pp. 277–294.

[8]Swartz, S. M., Bishop, K. L., and Ismael-Aguirrre, M.-F., "Dynamic Complexity of Wing Form in Bats: Implications for Flight Performance," *Functional and Evolutionary Ecology of Bats*, Oxford University Press, Oxford, UK, 2005.

[9]Dickinson, M. H., Lehmann, F. O., and Sane, S. P., "W," Vol. 207, 1999, pp. 4269–4281, B. Dickinson and M. H. Dickinson, "The effect of advance ratio on the aerodynamics of revolving wings," *Journal of Experimental Biology*.

[10]Ellington, C., "The Aerodynamics of Hovering Insect Flight. I-VI," *Philosophical Transactions of the Royal Society of London B Biological Sciences*, Vol. 305, 1984, 1181, .

[11]Hall, K. C., Pigott, S. A., and Hall, S. R., "Power Requirements for Large-amplitude Flapping Flight," *Journal of Aircraft*, Vol. 35, No. 3, 1998, pp. 352–361.

[12]Willis, D. J., Peraire, J., Drela, M., and White, J. K., "A Numerical Exploration of Parameter Dependence in Power Optimal Flapping Flight," 2006, pp. 2006–2994, AIAA.

[13]Wang, Z. J., "Aerodynamic Efficiency of Flapping Flight: Analysis of a Two-stroke Model," *The Journal of Experimental Biology*, Vol. 211, 2008, pp. 234–238.

[14]B. Roget, J. Sitaraman, R. H. J. G. J. C. J. H. and Humbert, S., "A Computational Study of Flexible Wing Ornithopter Flight," *Proc. of the 26th Applied Aerodynamics Conference*, 2008, Honolulu, HI, AIAA 2008-6397.

[15]R. J. Albertani, B. Stanford, R. D. J. P. H. and Ifju, P., "Wind-tunnel Testing and Modeling of a Micro Air Vehicle with Flexible Wings," *Journal of Aircraft*, Vol. 35, No. 3, 2008, pp. 1025–1032.

[16]Ho, S., Nassef, H., Pornsinsirirak, N., T., Y.-C., and Ho, C.-M., "Unsteady Aerodynamics and Flow Control for Flapping Wing Flyers," Vol. 39, 2003, Progress in Aerospace Sciences 635681.

[17]Swartz, S. M., Iriarte-Diaz, J., Riskin, D. K., Song, A., Tian, X., Willis, D. J., and Breuer, K. S., "Wing Structure and the Aerodynamic Basis of Flight in Bats," *Proc. of the 45th AIAA Aerospace Science Meeting*, 2007, Reno NV.

[18]X. Tian, K. Breuer, e. a., "Direct Measurements of the Kinematics and Dynamics of Bat Flight," *Bioinsp. Biomim.*, Vol. 1, 2006, S10-S19.

[19]Deng, X., Schenato, L., Wu, W. C., and Sastry, S. S., "Flapping Flight for Biomimetic Robotic Insects: Part I-system Modeling," *IEEE Trans. on Robotics*, Vol. 22, No. 4, 2006, pp. 776–788.

[20]Deng, X., Schenato, L., Wu, W. C., and Sastry, S. S., "Flapping Flight for Biomimetic Robotic Insects: Part II-flight Control Design," *IEEE Trans. on Robotics*, Vol. 33, No. 4, 2006, pp. 789–803.

[21]Frampton, K. D., Goldfarb, M., Monopoli, D., and Cveticanin, D., "Passive Aeroelastic Tailoring for Optimal Flapping Wings," *Fixed and Flapping Wing Aerodynamics for Micro Air Vehicle Application*, 2001, pp. 473–482, T. J. Mueller, Ed., AIAA,.

[22]Issac, K. K. and Agrawal, S. K., "An Investigation Into the Use of Springs and Wing Motions to Minimum the Power Expended by a Pigeon-sized Mechanical Bird for Steady Flight," *Journal of Mechanical Design, Transactions of the ASME*, Vol. 129, 2007, .

[23]Jones, K. D., Lund, T. C., and Platzer, M. F., "Experimental and Computational Investigation of Flapping Wing Propulsion," *Fixed and Flapping Wing Aerodynamics for Micro Air Vehicle Application*, 2001, pp. 307–336, T. J. Mueller, Ed., AIAA,.

[24]Kawamura, Y., Souda, S., Nishimoto, S., and Ellington, C. P., "Clapping-wing Micro Air Vehicle of Insect Size," *Bio-Mechanisms of Swimming and Flying: Fluid Dynamics, Biomimetic Robots, and Sports Science*, Springer Verlag, 2008, pp. 319–330, N. Kato and S. Kamimura, Ed.

[25]Larijani, R. F. and DeLaurier, J. D., "A Nonlinear Aeroelastic Model for the Study of Flapping Wing Flight," *Fixed and Flapping Wing Aerodynamics for Micro Air Vehicle Application*, AIAA, 2001, pp. 399–428, T. J. Mueller, Ed.

[26]Michelson, R., Helmick, D., Reece, S., and Amarena, C., "A Reciprocating Chemical Muscle (RCM) for Micro Air Vehicle Entomopter Flight," *Proc. of the Association for Unmanned Vehicle Systems, International*, 1997, pp. 429–435.

[27]Steltz, E., Avadhanula, S., and Fearing, R. S., "High Lift Force with 275 Hz Wing Beat in MFI," *IEEE Int. Conf. on Intelligent Robots and Systems*, 2007, San Diego, CA.

[28]Wood, R. J., "The First Takeoff of a Biologically-inspired At-scale Robotic Insect," *IEEE Trans. on Robotics*, Vol. 24, No. 2, 2008, pp. 341–347.

[29]Taylor, G. K. and Zbikowski, R., "Nonlinear Time-periodic Models of the Longitudinal Flight Dynamics of Desert Locusts Schistocerca Gregaria," *J. R. Soc. Interface*, Vol. 2, 2005, pp. 197–221.

[30]Zbikowski, R., Ansari, S. A., and Knowles, K., "On Mathematical Modelling of Insect Flight Dynamics in the Context of Micro Air Vehicles," *Bioinsp. Biomim.*, Vol. 1, 2006, pp. 26–37.

[31]Birch, J. and Dickinson, M., "Spanwise Flow and the Attachment of the Leading-edge Vortex on Insect Wings," *Nature*, Vol. 412, Aug . 2001, pp. 729–733.

[32]T. Pornsinsirirak, S-W. Lee, H. N. J. G. Y.-C. T. C.-M. H. M. K., "MEMS Wing Technology for a Battery-powered Ornithopter," *Proceedings of the International Conferences on MEMS*, 2000, pp. 709–804, Miyazaki, Japan.

[33]Jadhav, G., *The Development of a Miniature Flexible Flapping Wing Mechanism for Use in a Robotic Air Vehicle*, 2007, M.S. Thesis, Georgia Institute of Technology, Atlanta, GA.

[34]Bay, J. S. and Hemami, H., "Modeling of a Neural Pattern Generator with Coupled Nonlinear Oscillators," *IEEE Trans. on Biomedical Engineering*, 1987.

[35]Bernstein, N., *The Coordination and Regulation of Movements*, Pergamon Press, Oxford, 1967.

[36]Collins, J. J. and Stewart, I. N., "Coupled Nonlinear Oscillators and the Symmetries of Animal Gaits," *Nonlinear Science*, Vol. 3, 1993, pp. 349–392.

[37]Golubitsky, M., Stewart, I., Buono, P., and Collins, J., "Symmetry in Locomotor Central Pattern Generators and Animal Gaits," *Nature*, Vol. 401, No. 19, 1999, pp. 693–695.

[38]Hooper, S. L., "Central Pattern Generators," *In Nature Encyclopedia of Life Sciences*, 2001, London, Nature Publishing Group.

[39]Hooper, S. L., Guschlbauer, C., von Uckermann, G., and Buschges, A., "Natural Neural Output That Produces Highly Variable Locomotory Movements," *J. Neurophysiology*, Vol. 96, 2006, pp. 2072–2088.

[40]Lewis, M. A., Tenore, F., and Etienne-Cummings, R., "CPG Design Using Inhibitory Networks," *Proc. of the 2005 IEEE Int'l Conference on Robotics and Automation*, 2005, pp. 3682–3687, Barcelona, Spain.

[41]Matsuoka, K., "Mechanisms of Frequency and Pattern Control in Neural Rhythm Generators," *Biological Cybernetics*, Vol. 56, 1987, pp. 345–353.

[42]Sekerli, M. and Butera, R. J., "Oscillations in a Simple Neuromechanical System: Underlying Mechanisms," *Journal of Computational Neuroscience*, Vol. 19, No. 2, 2005, pp. 181–197.

[43]Marder, E. and Calabrese, R. L., "Principles of Rhythmic Motor Pattern Production," *Physiological Reviews*, Vol. 76, 1996, pp. 687–717.

[44]Grillner, S., "Neurological Bases of Rhythmic Motor Acts in Vetebrates," *Science*, Vol. 228, 1985, pp. 143–149.

[45]Zheng, T. I. M., "Sensory Feedback Mechanism Underlying Entrainment of Central Pattern Generator to Mechanical Resonance," *Biological Cybernetics*, Vol. 94, No. 4, 2006, pp. 245–261.

[46]Seo, K., Chung, S.-J., and Slotine, J.-J. E., "CPG-based Control of a Turtle-like Underwater Vehicle," *Proc. of the Robotics: Science and Systems (RSS)*, 2008, Switzerland.

[47]Ijspeert, A. J., "Central Pattern Generators for Locomotion Control in Animals and Robots: A Review," *Neural Networks*, Vol. 24, No. 4, 2008, pp. 642–653.

[48]Ayers, J. and Rulkov, N., "Controlling Biomimetic Underwater Robots With Electronic Nervous Systems," *Bio-Mechanisms of Swimming and Flying: Fluid Dynamics, Biomimetic Robots, and Sports Science*, Springer Verlag, 2008, pp. 295–306, N. Kato and S. Kamimura, Ed.

[49]Ijspeert, A. J., Crespi, A., and Cabelguen, J.-M., "Simulation and Robotics Studies of Salamander Locomotion: Applying Neurobiological Principles to the Control of Locomotion in Robots," *Neuroinformatics*, Vol. 3, No. 3., 2005, pp. 171–195.

[50]Morimoto, J., Endo, G., Nakanishi, J., and Cheng, G., "A biologically inspired biped locomotion strategy for humanoid robots: modulation of sinusoidal patterns by a coupled oscillator model," 2006.

[51]Strogatz, S., *Nonlinear Dynamics and Chaos With Applications to Physics , Biology, Chemistry, and Engineering*, Perseus Books Group, Cambridge, MA, 1994.

[52]Slotine, J.-J. E. and Li, W., *Applied Nonlinear Control*, Prentice Hall, 1991.

[53]Pham, Q.-C. and Slotine, J.-J. E., "Stable Concurrent Synchronization in Dynamic System Networks," *Neural Networks*, Vol. 20, No. 1, 2007, pp. 62–77.

[54]Chung, S.-J. and Slotine, J.-J. E., "On Global Synchronization of Coupled Hopf-Kuramoto Nonlinear Oscillators," 2009, submitted.

[55]Norberg, U. M. and Winter, Y., "Wing Beat Kinematics of a Nectar-feeding Bat, Glossophaga Soricina, Flying At Different Flight Speeds and Strouhal Numbers," *J. of Experimental Biology*, Vol. 209, 2006, pp. 3887–3897.

[56]Taga, G., "A Model of the Neuro-musculo-skeletal System for Anticipatory Adjustment of Human Locomotion During Obstacle Avoidance," *Biological Cybernetics*, Vol. 78, No. 1, 1998, pp. 9–17.

[57]Doya, K., Kimura, H., and Kawato, M., "Neural Mechanisms of Learning and Control," *IEEE Control Systems Magazine*, Vol. 21, No. 4, 2001, pp. 42–54.

[58]Riskin, D. K., Willis, D. J., Iriarte-Diaz, J., Hendrick, T. L., Kostandov, M., Chen, J., Laidlaw, D. H., Breuer, K. S., and Swartz, S. M., "Quantifying the Complexity of Bat Wing Kinematics," *J. of Theoretical Biology*, Vol. 254, 2008, pp. 604–615.

[59]Chung, S.-J. and Slotine, J.-J. E., "Cooperative Robot Control and Concurrent Synchronization of Lagrangian Systems," *IEEE Transactins on Robotics*, Vol. 25, No. 3, 2009.

[60]Lohmiller, W. and Slotine, J.-J. E., "Contraction Analysis for Nonlinear Systems," *Automatica*, Vol. 34, No. 6, 1998, pp. 683–696.

[61]Iwasaki, T. and Zheng, M., "What Makes Biological Oscillators Achieve Robust Self-excitation?" Vol. 2, 2003, pp. 1824–1829, Proc. American Control ConferenceJune .

[62]Taga, G., Yamaguchi, Y., and Shimizu, H., "Self-organized Control of Bipedal Locomotion by Neural Oscillators in Unpredictable Environment," *Biological Cybernetics*, Vol. 65, 1991, pp. 147–159.

[63]Ijspeert, A. J., Crespi, A., Ryczko, D., and Cabelguen, J.-M., "From Swimming to Walking with a Salamander Robot Driven by a Spinal Cord Model," *Science*, Vol. 315, No. 5817, 2007, pp. 1416–1420.

[64]Morimoto, J., Endo, G., Nakanishi, J., Hyon, S.-H., Cheng, G., Bentivegna, D., and Atkeson, C. G., "Modulation of Simple Sinusoidal Patterns by a Coupled Oscillator Model for Biped Walking," *Proc. of the 2006 IEEE Int'l Conference on Robotics and Automation*, 2006, pp. 1579–1584.

[65]MacMahon, T. A., *Muscles, Reflexes, and Locomotion*, 1984, Princeton University Press, .

[66]Thomas, A. L. R. and Taylor, G. K., "Animal Flight Dynamics I. Stability in Gliding Flight," *J. Theor. Biol.*, Vol. 212, 2001, pp. 399–424.

[67]Taylor, G. K. and Thomas, A. L. R., "Animal Flight Dynamics II. Longitudinal Stability in Flapping Flight," *J. theor Biol.*, Vol. 214, No. 3, February 2002, pp. 351–370.

[68]Swartz, S. M., Groves, M. S., Kim, H. D., and Walsh, W. R., "Mechanical Properties of Bat Wing Membrane Skin," *Journal of Zoology*, Vol. 239, 1996, pp. 357–378.